White Rose Research Online
eprints@whiterose.ac.uk
https://eprints.whiterose.ac.uk
Universities of Leeds, Sheffield and York

Deposited via The University of Leeds.

White Rose Research Online URL for this paper:
https://eprints.whiterose.ac.uk/id/eprint/236418/

Version: Accepted Version

Article:

Zhou, Q., Song, Y., Gan, K. et al. (2026) Coupling X-ray absorption spectroscopy and chemical extractions to investigate phosphorus phase partitioning in Ningxiang iron deposits. Geochimica et Cosmochimica Acta. ISSN: 0016-7037

https://doi.org/10.1016/j.gca.2026.01.012

This is an author produced version of an article published in Geochimica et Cosmochimica Acta, made available via the University of Leeds Research Outputs Policy under the terms of the Creative Commons Attribution License (CC-BY), which permits unrestricted use, distribution and reproduction in any medium, provided the original work is properly cited.

Reuse

This article is distributed under the terms of the Creative Commons Attribution (CC BY) licence. This licence allows you to distribute, remix, tweak, and build upon the work, even commercially, as long as you credit the authors for the original work. More information and the full terms of the licence here: https://creativecommons.org/licenses/

Takedown

If you consider content in White Rose Research Online to be in breach of UK law, please notify us by emailing eprints@whiterose.ac.uk including the URL of the record and the reason for the withdrawal request.

UNIVERSITY OF LEEDS
University of Sheffield
UNIVERSITY of York

Coupling X-ray absorption spectroscopy and chemical extractions to investigate phosphorus phase partitioning in Ningxiang iron deposits

Qiang Zhou[a,b,1], Yafang Song[b,1], Kai Gan[a], Yijun Xiong[c], Than Dam[d], Mengqiang Zhu[d], Changzhi Wu[e], Jihua Hao[b], Simon W. Poulton[c], Wei Li[a]*

[a] State Key Laboratory of Critical Earth Material Cycling and Mineral Deposits, Key Laboratory of Surficial Geochemistry (Ministry of Education), Frontiers Science Center for Critical Earth Material Cycling (FSC-CEMaC), School of Earth Sciences and Engineering, Nanjing University, Nanjing 210023, China

[b] Deep Space Exploration Laboratory/State Key Laboratory of Lithospheric and Environmental Coevolution, University of Science and Technology of China, Hefei 230026, China

[c] School of Earth, Environment and Sustainability, University of Leeds, Leeds LS2 9JT, UK

[d] Department of Ecosystem Science and Management, University of Wyoming, Laramie, WY 82071

[e] Key Laboratory of Western China's Mineral Resources and Geological Engineering, Ministry of Education, School of Earth Science and Resources, Chang' an University, Xi'an 710054, China

[1] These authors contributed equally to the manuscript

* Corresponding author: Wei Li, Email: liwei_isg@nju.edu.cn, Phone: 8625-89681539

Abstract

Phosphorus (P) is the ultimate limiting nutrient for primary productivity on geological timescales, but reconstructing ancient seawater phosphate concentrations in iron-rich sediments is complicated by post-depositional transformations that may obscure primary P signatures. Here, we investigate phosphorus phase partitioning in Late Devonian Ningxiang oolitic ironstones from South China, using a combined approach integrating sequential chemical extractions, solid-state ^{31}P nuclear magnetic resonance (SSNMR), and P *K-edge* X-ray absorption near-edge structure (XANES) spectroscopy. The ironstones, composed mainly of hematite, exhibit systematically higher P contents than their siliciclastic host rocks. Our results reveal pronounced stratigraphic variability in P phases: Al/Fe-bound P dominates in the Huangjiadeng Formation, whereas authigenic Ca-phosphates (apatite and carbonate-fluorapatite) prevail in the overlying Xiejingsi Formation. This transition reflects diagenetic transformation of primary Fe-P phases under progressively reducing pore-water conditions, followed by re-precipitation as stable Ca-phosphate minerals. Spectroscopic analyses reveal that Al-bearing minerals constitute a significant, yet previously underappreciated, sink for phosphorus. This redistribution of P among Fe-, Al- and Ca-bound phases challenges the conventional use of bulk P/Fe ratios in Phanerozoic ironstones as direct proxies for paleo-seawater phosphate concentrations. Our study demonstrates that coupling XAFS and NMR spectroscopy with sequential extractions provides a powerful approach to resolve phosphorus phase partitioning and cycling in ancient marine settings.

Keywords: oolitic ironstone; Devonian; phosphorus phase partitioning; Al-bound P minerals; oceanic redox conditions; XAFS; XANES; NMR; seawater phosphate concentrations

1. Introduction

Phosphorus (P) is an essential macronutrient for life because of its critical role in the formation of genetic materials (DNA and RNA), mediating energy transfer (via ATP), and constructing lipid membranes (e.g., Defforey and Paytan, 2018; Westheimer, 1987). On geological timescales, phosphorus is widely regarded as the ultimate limiting nutrient for primary producers (Tyrrell, 1999). Consequently, the bioavailability of P in the ocean regulated primary productivity, organic carbon burial, and ultimately oxygen production, across extended intervals of Earth's history (Alcott et al., 2022; Bjerrum and Canfield, 2002; Guilbaud et al., 2020; Planavsky et al., 2010; Reinhard et al., 2017).

In the marine realm, the bioavailability of P is principally controlled by inputs to the ocean and outputs to sediments (Ruttenberg, 2014). The dominant source of P is through transport from continents to the ocean via rivers, while the principal P sinks comprise sedimentary burial in association with organic matter (P_{org}), iron minerals (P_{Fe}), authigenic minerals (P_{auth}) and detrital apatite (P_{det}) (e.g., Paytan and McLaughlin, 2007; Ruttenberg, 2014). Previous studies have demonstrated that P sequestration and regeneration are highly redox dependent (e.g., Ingall et al., 1993; Ingall and Jahnke, 1994). For example, under anoxic conditions, P can be released through the degradation of organic matter or the reductive dissolution of Fe (oxyhydr)oxides. This released P may then undergo 'sink-switching' to authigenic phases, including carbonate fluorapatite (CFA) or vivianite, in addition to re-adsorption to Fe (oxyhydr)oxides (Jilbert and Slomp, 2013; Ruttenberg and Berner, 1993; Slomp et al., 1996; Van Cappellen and Ingall, 1994; Xiong et al., 2019). However, a proportion of the P released during diagenesis may also be recycled back to the water column, where it may promote further productivity (e.g., Ingall and Jahnke, 1994; 1997; Slomp et al., 2002; 2004). This process may be particularly significant under euxinic water column conditions or under ferruginous water column conditions where porewaters are sulfidic close to the sediment-water interface (e.g., Alcott et al., 2022; Qiu et al., 2022).

Understanding the role of diagenesis in controlling P cycling in Fe-rich chemical sediments is, however, poorly constrained, although previous work has demonstrated the potential for extensive ‘sink-switching’ in some settings (Konhauser et al., 2007; Poulton and Canfield, 2006; Schad et al., 2021). However, our understanding of how diagenesis modifies P phase partitioning in Phanerozoic ironstones is particularly limited, due to a lack of studies that directly characterize P phases, rather than simply inferring host phases from bulk ratios.

To address these knowledge gaps, sequential extraction techniques (e.g., the SEDEX scheme and its modifications; Ruttenberg, 1992; Thompson et al., 2019) have been widely employed to quantify operationally-defined sedimentary P pools, greatly advancing our understanding of ancient P cycling (e.g., Guilbaud et al., 2020; Qiu et al., 2022; Schobben et al., 2020; Song et al., 2023; Yang et al., 2024). However, these methods do not directly identify the mineralogical hosts or bonding environments of P, which are critical for understanding its diagenetic behaviour. Spectroscopic techniques can overcome this limitation. Specifically, ^{31}P solid-state nuclear magnetic resonance (SSNMR) spectroscopy is a non-destructive and element-specific technique, which can probe the local molecular bonding environment around P atoms, thereby enabling inorganic P phases (e.g., Ca-bound P, Al-bound P) to be distinguished based on unique chemical shifts (Kar et al., 2011; Li et al., 2012; Li et al., 2015; Mason et al., 2011; Prietzel et al., 2013). Additionally, P *K-edge* X-ray absorption near edge structure (XANES) spectroscopy complements SSNMR by detecting Fe-bound P (a phase that is difficult to detect with SSNMR; Negassa et al., 2010; Kizewski et al., 2011; Li et al., 2015; Liu et al., 2015). Therefore, the combined application of sequential chemical extractions and spectroscopic techniques offers a powerful approach to investigate P phase partitioning in sedimentary rocks.

The Late Devonian Ningxiang-type iron deposits in South China are a prime example of Phanerozoic ironstones, yet the phase associations and diagenetic cycling of P within these deposits remain poorly constrained. Here, we integrate sequential extractions and multi-spectroscopic analyses (XANES and SSNMR) to resolve phase-specific P distributions in the Ningxiang oolitic ironstones. Our two major objectives are: (1) to fully characterize the distribution of P phases and identify potential diagenetic transformations, and (2) to use comprehensive P phase association data to assess how phosphorus partitioning in ironstones may modify the applicability and reliability of bulk geochemical proxies (e.g., P/Fe ratios) for the reconstruction of ancient seawater phosphate concentrations.

2. Geological background

Oolitic ironstones (OISs) are iron-rich (>15 wt%) chemical sedimentary rocks that were commonly deposited during the Ordovician-Devonian and Jurassic-Paleogene (Bekker et al., 2010; Matheson and Pufahl, 2021). Typically, OIS is primarily composed of Fe- (e.g., hematite) and Si- (e.g., chamosite, berthierite) coated and cemented grains. The Devonian OIS samples used in this study were collected from the Huoshaoping area, Hubei Province, South China and are known as Ningxiang-type ironstones (**Fig. 1**). Ningxiang OISs are important iron resources (>3.72 billion tons of iron) that were widely deposited in shore to shelf environments (Liu et al., 2017; Zhou et al., 2024; **Fig. 1**). Four ironstone layers (named Fe_{I}, Fe_{II}, Fe_{III} and Fe_{IV}) occur within siliciclastic-carbonate rocks of the Late Devonian Huangjiadeng and Xiejingsi formations (**Fig. 2**). Based on the Late Devonian chronostratigraphy of China, the Huangjiadeng Formation (Hubei) and its equivalent Shetianqiao Formation (Hunan) were deposited during the Frasnian (383-372 Ma), whereas the Xiejingsi Formation and its equivalent Xikuangshan Formation were deposited during the Famennian (372-359 Ma) (Qie et al., 2018).

The Huangjiadeng Formation was deposited in a nearshore environment, as evidenced by its dominant lithology of thick sandstone and mudstone beds, which commonly contain sedimentary structures such as oblique bedding, cross-bedding, and ripple marks (**Fig. 2**; Gan et al., 2021; Ma and Zong, 2010). Within this formation, Fe_{I} and Fe_{II} occur as thin, discontinuous iron-rich layers (**Figs. 3A, B**). The Xiejingsi Formation was deposited in an offshore environment characterized by a mixture of limestones, oolitic ironstones and shales (**Fig. 2**; Gan et al., 2021; Ma and Zong, 2010). The lower Xiejingsi Formation is dominated by shales, with infrequent layers of quartz sandstones and silty mudstones. The upper Xiejingsi Formation consists of limestones and marls intermixed with siliciclastic rocks. Corals, brachiopods and molluscs are more common in the Xiejingsi Formation than in the Huangjiadeng Formation (**Fig. 2C**). The Fe_{III} and Fe_{IV} layers developed during deposition of the upper Xiejingsi Formation. The Fe_{III} layer is the main iron-bearing layer and can be further divided into Fe_{III}^{1}, Fe_{III}^{2} and Fe_{III}^{3} intervals **(Figs. 3C-G**).

3. Materials and Methods

3.1. Sampling

Twenty-one samples were collected, including two OIS samples from Fe_{I}, one from Fe_{II}, and one from Fe_{IV} (**Fig. 2**). The most iron-rich layer, Fe_{III}, was precipitated during transgression and regression cycles, and six samples were collected. In addition, 11 samples of fine-grained siliciclastic rocks were collected from the interlayers of these iron-rich layers. The sample naming convention is as follows: Fe_{m}^{n}-x, where ‘m’ is the main iron-bearing layer, ‘n’ is the sub-layer, and ‘x’ is the sample number.

3.2. Microscopy, XRD and SEM-EDS analysis

The morphology of the oolitic particles was observed by polarizing microscopy. Mineralogy was analysed via X-ray diffraction (XRD), while microstructures were analysed by scanning electron microscopy (SEM). XRD (Cu Kα radiation) data were collected via a Bruker (Germany) D2 Phaser at 10-80° 2θ with a step size of 0.2°. We used the powder diffraction files provided in MDI Jade 6.0 software to identify the mineralogy of the crystalline phases in the samples. To further investigate the elemental distributions of P and Fe, the samples were analysed via SEM (Sigma 500, Germany) with an energy dispersive spectrometer (SEM-EDS; Inca Energy 400, Oxford, UK). SEM-EDS elemental mapping was performed on carbon-coated samples using an accelerating voltage of 15 kV and a working distance of approximately 10 mm. Maps were acquired with a pixel resolution of 2048 × 1536 and a dwell time of 5 μs per pixel, resulting in a total acquisition time of approximately 15-20 seconds per map.

3.3. Major elements and organic carbon analyses

For total element and total organic carbon (TOC) analyses, samples were ground into fine powder (<200 mesh) via an agate mortar. Major element compositions (Ca, Al, P and Fe) were measured at the University of Leeds via Inductively Coupled Plasma-Optical Emission Spectrometry (ICP-OES, ThermoFisher iCAP 7400) on ashed samples that were subsequently dissolved with HF-HNO_3-$HClO_4$. Replicate major element analyses of the samples via ICP-OES yielded relative standard deviations (RSDs) of <2%, and accuracies greater than 90%, as determined by recovery rates following analyses of Brush Creek Shale (CBC-1). Before the analysis of TOC, ~0.5 g of sample powder was treated with 10 ml of 1 M HCl for 12 h to remove carbonate minerals. The samples were subsequently centrifuged at 10,000 rpm for 5 min before being washed with ultrapure water three times. TOC concentrations were measured on a Costech ECS 4024 CNHS-O Elemental Combustion Analyser at the Key Laboratory of Surficial Geochemistry, Nanjing University. Replicate analyses gave RSDs of <2% for each sample.

3.4. Phosphorus sequential extractions

The detailed steps for phosphorus sequential extractions are presented in **Fig. S1**. The solubility of P_{auth} may decrease during burial diagenesis due to recrystallization, and any recrystallized P_{auth} that was not extracted by Na acetate would likely be extracted as part of the detrital apatite pool (comprising igneous and metamorphic apatite minerals), which we term P_{cryst} (Thompson et al., 2019). The P phases extracted using sodium acetate and HCl solutions (P_{auth}, P_{cryst} and P_{org}) were determined spectrophotometrically via the molybdate-blue method on a Spectronic GENESYS™ 6 at 880 nm (Murphy and Riley, 1962), with replicate extractions giving RSDs of<5% for all phases (**Table S2**). The P phases extracted using citrate-dithionite-bicarbonate, ammonium oxalate and citrate-dithionite-acetate (P_{Fe1}, P_{Fe2} and P_{mag}) were analysed via ICP-OES due to colour interference with the molybdate blue method, with replicate extractions giving RSDs of<2% (**Table S2)**. The sum of the sequential P extraction steps (P_{sum}) was compared to the total P (P_{tot}) content to evaluate the recovery and reliability of the sequential extraction procedure. As detailed in **Table 2**, the recovery rates for the vast majority of samples exceeds 90%, with many surpassing 95%. The sole exception is sample Fe_I-2, which exhibits a lower recovery of 69%.

3.5. ^{31}P solid-state NMR spectroscopy

^{31}P solid-state NMR spectra for sample powders were obtained on a 400 MHz Bruker AVANCE III spectrometer at Nanjing University, using an operating frequency of 161.8 MHz for ^{31}P. A Bruker 4.0 mm HX double resonance probe was employed for all measurements. All samples were spun at a frequency of 14 kHz in a 4 mm o.d. ZrO rotor. The ^{31}P single pulse (SP/MAS) spectra were collected with a 90° pulse of 3 μs, with a 120 s relaxation delay. The ^{31}P chemical shifts were referenced to an external 85% H_3PO_4 solution, with hydroxyapatite as a secondary reference set to $\delta_{P\text{-}31}$ = 2.65 ppm. Approximately 300-30000 scans were collected for each sample to achieve a good signal-to-noise ratio.

3.6. Phosphorus *K-edge* XANES spectroscopy

Phosphorus *K-edge* XANES analyses were performed at beamline X15B at the National Synchrotron Light Source (NSLS), Brookhaven National Laboratory (Upton, NY), and the Soft X-ray Micro Characterization Beamline (SXRMB) at the Canadian Light Source, Saskatoon, Canada. At the SXRMB, the peak maximum of the first derivative spectrum of $AlPO_4$ (berlinite) was set at 2152.9 eV to calibrate the beamline energy. Further details of the data collection at the SXRMB are provided elsewhere (Dam et al., 2021). Prior to data collection, homogenized dry sediment powder was spread as a thin film in a custom-built sample holder, comprising an envelope made from a polyethylene membrane (with zero P background). The incident X-ray energy was calibrated against a standard (e.g., fluorapatite). The XANES spectra were collected in fluorescence mode in a He chamber at room temperature via a multichannel Ge detector. The spectra were further processed by averaging 25-40 scans to achieve a good signal-to-noise ratio. Data processing was performed using the ATHENA software package (Ravel and Newville, 2005).

3.7. Iron *K-edge* EXAFS spectroscopy

The EXAFS data for the Fe *K-edge* were acquired at the Beijing Synchrotron Radiation Facility (BSRF, China). The electron storage ring was operated at 2.5 GeV with an average beam current of 250 mA. Si (111) was used as the monochromator. The X-ray energy was calibrated using an iron metal foil, and the first inflection point in the Fe *K-edge* was set to 7112 eV. All spectra were collected in transmission mode at ambient temperature. The averaged spectra were background-subtracted, normalized, and finally converted to *k*-space, which was weighted by k^3. The contribution of different Fe phases to total Fe fitting was calculated via linear combination fitting (LCF) in the k^3 weighted χ-space (3-12 $Å^{-1}$) via the ATHENA software package (Ravel and Newville, 2005).

3.8. Sulfur *K-edge* XANES spectroscopy

The S *K-edge* XANES data were recorded in the energy range of 2450-2520 eV in fluorescence mode by a silicon drift detector (e2v, Chelmsford, UK) at beamline 4B7A, BSRF. For all edge-normalized spectra, the contributions of different S phases to the total S content were calculated using LCF carried out in the energy range of 2465-2500 eV via routine LCF in ATHENA (Ravel and Newville, 2005). For LCF analysis of the mixtures, edge-normalized spectra of pyrite (FeS_2) and gypsum ($CaSO_4$) were used as predictor components.

4. Results

4.1. Petrographic analyses

The Fe_I layer, hosted in coarse-grained sandstones, is characterized by quartz clasts with moderate to poor roundness (**Fig. 4A**). The ooids in Fe_I, ranging from 0.2 to 0.5 mm in diameter, exhibit concentric lamination, and their nuclei generally comprise argillaceous aggregates or quartz clasts (**Fig. 4A**). No ooids were observed in Fe_{II}, where iron minerals (hematite) preferentially cement around quartz grains (**Fig. 4B**). No fossils were observed in Fe_I or Fe_{II}. Moving upwards, the Fe_{III} layer is hosted within shale and limestone, which is different from the sandstone host rocks for Fe_I and Fe_{II} (**Fig. 2**). The ooids in Fe_{III}^1 also exhibit concentric lamination, with diameters ranging from 0.2 to 0.5 mm (**Fig. 4C**), and the nuclei generally consist of quartz clasts (**Fig. 4C, 4H**). Abundant shallow marine fossils (e.g., corals, echinoderms and gastropods) were found in $Fe_{III}1$ (**Figs. 2C, 3D and 4D**). The ooids in the $Fe_{III}2$ and $Fe_{III}3$ layers vary from spheroidal to elliptical and elongated, and are notably abundant (**Fig. 4E, 4H**). In addition, these ooids also exhibit variable diameters, ranging from 0.3-0.5 mm to 0.5-0.8 mm (**Fig. 4E, 4H**). Fossils in $Fe_{III}2$ are dominated by gastropods, echinoderms, bryozoans and ostracods (**Figs. 2C, 4F**). Notably, ooids infill the body cavities of some fossils (**Fig. 4F**). Compared with $Fe_{III}1$ **(Figs. 2C, 4D)**, there are no corals and less detrital materials in $Fe_{III}2$ and $Fe_{III}3$ **(Figs. 2C, 4E and 4H)**. The Fe_{IV} layer is hosted in limestone beds (**Fig. 3H**). Ooids in this layer are characterized by predominant bioclastic nuclei (ostracod fragments) and thin-laminated cortex, forming their unique amorphous morphology **(Fig. 4I)**. It is noteworthy that the ooid content in Fe_{IV} (around 50%) is significantly higher than the other ironstone layers, and the distribution of ooid grains in Fe_{IV} is relatively homogeneous (**Fig. 4I**).

The XRD analyses reveal that these OIS samples are predominantly composed of hematite, chamosite and quartz (**Fig. 5**), consistent with previous studies (Liu et al., 2017; Zhu, 2021). In addition, calcite and apatite were also detected in ironstone samples from the Fe_{III} and Fe_{IV} layers (**Fig. 5**). However, specific Fe-P mineral phases were not identified by XRD, likely due to their low concentration (<3 wt%) and/or poor crystallinity. As determined by SEM-EDS **(Fig. 6**), major elements in the OIS sediments are characteristically distributed in concentric laminae. A coherent distribution pattern of P and Fe was observed in Fe_I-2 (**Fig. 6A**), whereas P occurs synchronously with Ca rather than Fe in $Fe_{III}{}^3$-2 (**Fig. 6B**). Such an elemental distribution pattern is consistent with mineralogical results demonstrating that calcite is present only at trace levels in Fe_I-2 (0.18 wt%), while quartz cementation is more prevalent. By contrast, calcite cement was more frequently observed in Fe_{III} and Fe_{IV}. The combined SEM-EDS and XRD analyses suggest that the cortex of the ooids in Fe_I-2 is dominantly composed of hematite and clay minerals (e.g., chamosite and kaolinite), while the nucleus consists mainly of quartz or ooid clasts (**Fig. 6A**). By contrast, the cortex of the ooids in $Fe_{III}{}^3$-2 is dominantly composed of hematite and collophane, with quartz grains forming the nucleus, which is predominantly surrounded by chamosite (**Fig. 6B**).

4.2. Major element and TOC compositions

The OIS samples have high Fe contents ranging from 10.51 to 56.24 wt% (35.27 wt% on average), with total P (P_{tot}) contents ranging from 0.02 to 2.38 wt% (0.92 wt% on average) (**Fig. 7; Table 1**). Both Fe and P_{tot} concentrations in the OIS samples are predominantly higher than average upper continental crust values (Fe = 3.5 wt%, P = 0.07 wt%; McLennan, 2001). The contents of Al and Ca in the OIS samples are highly variable, ranging from 0.83 to 5.69 wt% for Al, and 0.02 to 26.35 wt% for Ca. Notably, even for Fe_I-2 and Fe_{III}^3-2, which have the highest Al contents (>3 wt%), their Al contents are lower than the average upper continental crust value (8.04 wt%; McLennan, 2001). Ca contents in Fe_{III} and Fe_{IV} (13.46 wt% on average) are considerably higher than those of Fe_I and Fe_{II} (0.10 wt% on average). Notably, Ca contents in Fe_{IV}-1 and Fe_{III}^3-1 are as high as ~26 wt%, significantly higher than the upper continental crust value (3 wt%; McLennan, 2001).

Fe contents of the interlayer samples range from 1.14 to 10.22 wt% (5.23 wt% on average), and P contents range from 0.01 to 0.75 wt% (0.19 wt% on average). Both Fe and P contents in the interlayer samples are lower than those of the OIS samples, and are closer to those of upper continental crust. The Al and Ca compositions of the interlayer samples are quite different to those of the OIS samples, with generally higher Al contents, ranging from 1.68 to 12.11 wt% (8.18 wt% on average), and mostly lower Ca contents, ranging from 0.02 to 7.93 wt% (1.81 wt% on average), with Ca contents for the interlayer samples being close to upper continental crust. Generally, samples from the interlayers have lower Ca, Fe and P_{tot} contents, but higher Al contents, compared to the OIS samples. Both the OIS and interlayer samples have low TOC contents, ranging from 0.05 to 0.35 wt% (**Fig. 7; Table 1**).

4.3. P sequential extraction data

The results of the P phase partitioning extractions are summarized in **Fig. 8** and **Table 2**. The P_{auth} and P_{cryst} concentrations are low in the Huangjiadeng Formation (26 ppm and 6 ppm on average, respectively) and increase to significantly higher values in the Xiejingsi Formation (2679 ppm and 2498 ppm on average). There is also a large difference between the OIS samples and interlayer samples in terms of P_{auth} and P_{cryst} concentrations. Specifically, the P_{auth} and P_{cryst} contents of the OIS samples (4679 ppm and 4543 ppm on average) are much higher than those of the interlayer samples (930 ppm and 709 ppm on average) in the Xiejingsi Formation.

Anomalously high P_{Fe} concentrations are observed in one oolitic OIS sample (Fe_{I} -2: 911 ppm) and in two interlayer samples (IL-5: 1397 ppm; IL-10: 2598 ppm). By contrast, OIS samples from the Xiejingsi Formation exhibit relatively low P_{Fe} concentrations (322 ppm on average) despite high total Fe contents (38.3 wt% on average). In the Huangjiadeng Formation, P_{Fe} accounts for more than 47% of total P in most samples (except Fe_{I}-2), whereas in the Xiejingsi Formation, P_{Fe} represents only 2.6-7.7% of total P (average 4.7%). Although the proportion of P_{Fe} increases to an average of 33.4% in interlayer samples from the Xiejingsi Formation, it is still lower than samples from the Huangjiadeng Formation. P_{org}

concentrations are also variable but generally low (ranging from 6 to 220 ppm), except for Fe_I-2, which shows an exceptionally high value of 3971 ppm (**Fig. 8E; Table 2**). P_{org} accounts for 10.5-80.4% (39.2% on average) of total P in samples from the Huangjiadeng Formation. Notably, in the Xiejingsi Formation, the proportion of P_{org} is less than 1% in all OIS samples, but increases to 12.4% in interlayer samples. Together, these results reveal pronounced lithological contrasts in P partitioning between formations: Huangjiadeng samples are dominated by Fe- and organic-bound phosphorus, whereas Xiejingsi samples are comparatively depleted in both phases, despite high total Fe contents.

4.4. ^{31}P solid-state NMR analysis

^{31}P solid-state NMR can readily distinguish different phosphate phases (e.g., calcium phosphate vs. aluminium phosphate) based on the chemical shifts. Generally, all calcium phosphate minerals yield chemical shifts at –2 to 3 ppm (e.g., hydroxyl apatite [HAP, $Ca_5(PO_4)_3(OH)$], fluorapatite [FAP, $Ca_5F(PO_4)_3$], or carbonate fluorapatite [CFAP, $Ca_5(PO_4,CO_3,OH)_3F$]), whereas crystalline Al phosphate and surface precipitates usually generate more negative chemical shifts, from –10 to –20 ppm, due to shielding of the Al-O-P bonds (Cade-Menun, 2005; Li et al., 2013). For example, brazilianite [$NaAl_3(OH)_4(PO_4)_2$] yields a peak at $\delta_{P\text{-}31}$ = –10.2 ppm, wavellite [$Al_3(OH)_3(PO_4)_2$] yields a peak at –11 ppm, metavariscite [$AlPO_4 \cdot 2H_2O$] yields a peak at –13.2 ppm, variscite [$AlPO_4 \cdot 2H_2O$] yields a peak at –19 ppm, and phosphate surface precipitates on gibbsite or kaolinite yield a peak at –11.5 ppm (Li et al., 2013; Van Emmerik et al., 2007). In addition, previous NMR studies have revealed inner-sphere phosphate surface complexes at $\delta_{P\text{-}31}$ = 0 and –6 ppm on boehmite (Li et al., 2010), $\delta_{P\text{-}31}$ = –3 ppm on γ-alumina (Johnson et al., 2002), $\delta_{P\text{-}31}$ = –6 ppm on amorphous $Al(OH)_3$ (Lookman et al., 1994), and $\delta_{P\text{-}31}$ = –4.5 ppm on gibbsite or kaolinite (Van Emmerik et al., 2007).

The ^{31}P chemical shift presented in **Fig. 9** increases gradually from negative (Fe_I) to positive (Fe_{III} and Fe_{IV}) values, reflecting the transformation from Al-P to Ca-P. Due to the relatively lower P contents (**Table 1**), the signal-to-noise ratios for $Fe_{III}{}^1$-1, $Fe_{III}{}^1$-2 and Fe_{IV}-1 are lower than those of the other samples, even after long scanning times. Similarly, there is no NMR signal for Fe_{II}-1 because of its extremely low P content (0.02 wt%). A dominant peak at 2.6 ppm is clearly observed for samples from the Fe_{III} and Fe_{IV} layers which can be assigned to apatite group minerals. For Fe_I-1 and Fe_I-2, negative dominant peaks at –11 and –5 ppm are observed, corresponding to Al-phosphate and adsorbed inner-sphere phosphate species on the surface of clay minerals, respectively. Because measuring Fe-bearing compounds is challenging in NMR analysis, identification of Fe-P minerals such as vivianite and strengite is unlikely; therefore, P *K-edge* XANES spectra were obtained in the following section to compensate for this limitation.

4.5. Phosphorus *K-edge* XANES

XANES data were collected for P-containing reference minerals and selected OIS samples (**Fig. 10**). We considered numerous naturally occurring P-containing minerals, laboratory-prepared P adsorption samples, and Fe oxide phases that are likely present in our samples. The iron phosphate (Fe-P) reference minerals (amorphous $FePO_4$, phosphate absorbed on ferrihydrite, and strengite) have similar post-edge and pre-edge features at 2150 eV (**Fig. 10A**), due to the presence of Fe^{3+} in these minerals. Pre-edge features cannot be observed in Fe^{2+} phosphate minerals (e.g., vivianite), unless they are partially oxidized (Brandes et al., 2007; Giguet-Covex et al., 2013). In addition, the white line position of the strength of ferric phosphate minerals is located at a higher energy than that of ferrous phosphate minerals because of binding to the Fe^{3+} phases. Apatite group minerals (Ca-P), such as superphosphate, octacalcium phosphate and hydroxyapatite, have two post-edge resonances between 2161 and 2182 eV, with peaks at 2164 and 2170 eV. In more detail, octacalcium phosphate and hydroxyapatite have a shoulder peak at 2155 eV, whereas other apatite group minerals do not (**Fig. 10A**), probably due to differences in the degree of crystallinity (Ravel and Newville, 2005). The P *K-edge* XANES spectra for Al-P differ significantly in terms of the broad features between 2165 and 2180 eV (**Fig. 10A**), which reflects a slight difference in the Al:P stoichiometry.

The spectra of Fe_{I} and Fe_{II} resemble the spectra of the Fe-P and Al-P reference materials, whereas those of Fe_{III} and Fe_{IV} are similar to those of the Ca-P standards (**Fig. 10B**). The P *K-edge* XANES spectra were fitted via a linear least-squares fitting method (**Fig. 10B**). The data analysis confirms that Al-P and Fe-P are major mineral components of Fe_{I} and Fe_{II}, whereas Ca-P is predominant in Fe_{III} and Fe_{IV}. Specifically, Al-P and Fe-P are major components of Fe_{I} and Fe_{II} (the sum of Al-P and Fe-P is ~87% on average, **Fig. 10C; Table S1**), but their proportions decrease significantly in Fe_{III} and Fe_{IV} (~34% on average, **Fig. 10C; Table S1**). Conversely, the Ca-P contents increase up-section (**Fig. 10C**), from average values of ~14% for Fe_{I} and Fe_{II}, to 66% for both Fe_{III} and Fe_{IV} (**Table S1**).

4.6. Iron *K-edge* EXAFS

Fe *K-edge* EXAFS was also conducted in this study because P chemistry is often coupled to Fe in marine sediments, and Fe mineralogy provides useful information for understanding the transformation of Fe-bearing minerals in response to anoxia and other environmental conditions, as well as for retaining or releasing P from deposited sediments (Follmi, 1996). However, the spectra of our OIS samples are generally similar, especially in the low-*K* range (**Fig. 11B**). This similarity suggests that these OIS samples likely contain similar types of Fe minerals. According to Liu et al. (2017), Ningxiang-type iron deposits contain five major Fe-containing minerals: hematite (Fe_2O_3), magnetite (Fe_3O_4), pyrite (FeS_2), siderite ($FeCO_3$) and chamosite ($((Fe,Mg)_3(Fe,Fe)_3[AlSi_3O_{10}](OH)_3)$). Here, we used reference spectra of hematite, magnetite, pyrite, siderite and vivianite ($Fe_3(PO_4)_2 \cdot 8H_2O$) to fit the *K-edge* EXAFS spectra of our samples.

Our results indicate that hematite is the major Fe mineral in all samples (**Fig. 11C**), accounting for 80-90% of the total Fe (**Table S1**). The proportion of vivianite tends to increase from Fe_I to Fe_{IV} (**Fig. 11C**), accounting for less than 10% in the Fe_I and Fe_{II} OIS layers, but more than 10% in the Fe_{III} and Fe_{IV} layers (**Table S1**). Magnetite was detected at a proportion of up to 13% in the Fe_I samples, whereas this phase accounted for no more than 7% in the remaining OIS samples (**Table S1**).

4.7. Sulfur *K-edge* XANES

We also conducted *K-edge* XANES analyses of S in our samples (**Fig. 12**). The white-line peaks of our samples are located mainly at 2471 and 2481 eV, consistent with signals from pyrite and gypsum, respectively (**Fig. 12A**). LCF was conducted to quantify the proportions of pyrite and gypsum (**Fig. 12B**). We analysed 10 samples (6 from OIS layers and 4 from interlayers), and the spectra of

Fe_I-2, IL-1, Fe_{II}-1 and $Fe_{III}{}^1$-2 were not fitted because of the obvious single gypsum white-line peak. In general, all samples from the Huangjiadeng Formation show a single peak at 2481 eV (Fe_I-2, IL-1 and Fe_{II}-1), whereas most samples from the Xiejingsi Formation have an additional peak at 2471 eV (IL-7, IL-9, $Fe_{III}{}^2$-2, $Fe_{III}{}^3$-1, IL-11 and Fe_{IV}-1), and the additional peak is stronger in the interlayer samples (IL-7, IL-9 and IL-11). These spectra indicate that interlayer samples from the Xiejingsi Formation (IL-7, IL-9 and IL-11) contain a large proportion of pyrite (ranging from 82 to 88%; **Fig. 12C**; **Table S1**). By contrast, the OIS samples from the Xiejingsi Formation ($Fe_{III}{}^1$-1, $Fe_{III}{}^2$-2, $Fe_{III}{}^3$-1, and Fe_{IV}-1) contain a large portion of gypsum (ranging from 69 to 100%; **Fig. 12C**; **Table S1**). Notably, some OIS samples from the upper Xiejingsi Formation ($Fe_{III}{}^2$, $Fe_{III}{}^3$ and Fe_{IV}) also contain pyrite (proportions ranging from 9 to 31%; **Fig. 12C**; **Table S1**) in addition to gypsum. It should be noted that the Fe-EXAFS LCF, while useful for identifying major Fe phases (>10%), is less sensitive to minor phases that may be unequivocally identified by more element-specific techniques, such as S-XANES.

5. Discussion

5.1. Comparison between chemical extractions and spectroscopic techniques

Both chemical extraction and spectroscopic techniques reveal consistent stratigraphic variability in phosphorus phase partitioning from the Huangjiadeng

Formation to the Xiejingsi Formation. As shown in **Fig.8** and **Table 2**, sequential extraction data show that the proportion of calcium-bound phosphorus (P_{Ca}) increases from a minor component (1.2-36.3%) in the Huangjiadeng Formation, to the dominant phosphorus pool in the Xiejingsi Formation (accounting for an average of 73.5% of total extractable P, and reaching 95.6% in oolitic ironstone samples). Conversely, the importance of iron-bound phosphorus (P_{Fe}) as a sink diminishes significantly, from often exceeding 47% of the phosphorus pool in the Huangjiadeng Formation, to a minor role (4.7% on average) in the OIS samples of the Xiejingsi Formation.

As shown in **Fig. 9**, negative peaks at −11 and −5 ppm are observed in the Fe_{I}-1 and Fe_{I}-2 samples by ^{31}P solid-state NMR spectroscopy, which can be assigned to Al-P signals. ^{31}P solid-state NMR revealed clear peaks at 2.6 ppm in the spectra of the Fe_{III} and Fe_{IV} samples, which suggests the presence of Ca-P minerals (Li et al., 2015). In addition, the detection via P *K-edge* XANES of a shoulder peak at 2155 eV in the Fe_{III} and Fe_{IV} samples (**Fig. 10B**) indicates that the specific apatite group mineral host is apatite or carbonate fluorapatite (CFA), which are the 'stable' end products of phosphogenesis and the main phases responsible for long-term P burial (Anderson et al., 2001; Zhao et al., 2020). Together, the combined P *K-edge* XANES and ^{31}P solid-state NMR data indicate that Al-P and Fe-P are the major P components of the Huangjiadeng Formation, whereas Ca-P is the predominant P pool in the Xiejingsi Formation.

One potential problem with evaluating the chemical partitioning of P is that authigenic CFA (i.e., P_{auth}) may transform into more highly crystalline apatite (i.e., P_{cryst}) during burial diagenesis and metamorphism, thus leading to an underestimation of the P_{auth} pool but an overestimation of the P_{cryst} pool (Thompson et al., 2019). The incomplete transformation of P_{auth} to P_{cryst} is a common phenomenon in sedimentary systems for several reasons. First, the transformation of metastable CFA to more stable crystalline apatite is a dissolution-reprecipitation process (Iacumin et al., 1996). At low temperatures characteristic of shallow burial diagenesis, this reaction can be slow (Ruttenberg et al., 2014; Ruttenberg and Berner, 1993). Second, chemical inhibition by porewater constituents (e.g., Mg^{2+}) is a well-known inhibitor of apatite crystallization (Yang et al., 2011), due to adsorption onto the growing surfaces of apatite crystals, which poisons growth sites and prevents further crystallization. Third, authigenic phosphate minerals can be encapsulated by other diagenetic phases, such as iron (oxyhydr)oxides (e.g., hematite) or clay minerals (Pufahl and Grimm, 2003). This physical coating creates a diffusion barrier, isolating the P_{auth} from the porewater and effectively halting any further chemical transformation or recrystallization.

To examine possible transformation between these two P phases, we consider the relationships between P_{auth} vs P_{cryst} and P_{cryst} vs Al (**Fig. S2**). There is a strong positive correlation between the P_{auth} and P_{cryst} contents (**Fig. S2**), suggesting that a higher concentration of P_{auth} may have been transformed to P_{cryst} when the primary P_{auth} content formed during early diagenesis was higher. This is supported by the lack of correlation between P_{cryst} and Al (**Fig. S2**), which suggests additional formation of P_{cryst} from the P_{auth} pool (Guilbaud et al., 2020). This transformation probably results in an underestimation of the P_{auth} fraction in our samples.

Our results highlight the advantage of spectroscopic techniques over traditional chemical extraction in directly identifying distinct phosphorus phases (e.g., Al-P, Fe-P and Ca-P). Both ^{31}P solid-state NMR and P *K-edge* XANES unambiguously identify Al-P in our samples (**Figs. 9, 10**). This phase cannot be resolved by chemical extractions alone. Indeed, it is unclear precisely where this phase would be dissolved in the chemical extraction scheme, since this would likely depend on the precise mineralogy of the Al-P phase, whereby some Al-rich clay minerals may be dissolved by the 1 M HCl extraction (see Raiswell et al., 1994) that targets P_{cryst} (**Fig. S1**), while more resistant phases would not be expected to be extracted by any of the sequential steps. Our results suggest that Al-P accounts for a considerable proportion of total P in Fe_I-1, Fe_I-2 and Fe_{II}-1, at a level comparable to or even greater than that of Fe-P (**Fig. 10C**; **Table S1**). This finding provides a new perspective to the sedimentary P cycle, demonstrating that while Ca-P and Fe-P are commonly considered the dominant authigenic phases (e.g., Paytan and McLaughlin, 2007; Ruttenberg, 2014), Al-bearing minerals such as glauconite may also play an important role as additional P hosts (Schobben et al., 2020).

Compared with the SEDEX extraction method, however, spectroscopic techniques suffer from an inherent limitation when applied to geological samples with low elemental concentrations. Either the element or phase of interest must be enriched, or substantially longer scan times are required. For example, satisfactory ^{31}P NMR spectra typically require P concentrations above ~1000 ppm, whereas samples with P concentrations <100 ppm may not yield viable results without weeks or even months of signal accumulation (Li et al., 2015). In our study, the low P content in Fe_{II}-1 generated a relatively poor signal-to-noise ratio even after many scans, giving a poor comparison between P *K-edge* XANES and chemical extraction data (**Figs. 8, 10**).

Despite their utility for identifying mineralogical host phases, both spectroscopic techniques and chemical extractions also have limitations when analysing organic-P phases. The P_{org} fraction determined by chemical extractions was not detected via spectroscopy because of the potential overestimation of P_{org} in the SEDEX extraction alongside spectroscopic limitations for P_{org} detection (**Table 2**). The SEDEX method operational defines P_{org} as the phosphorus released upon ignition at 550°C followed by HCl extraction. However, this step may also release phosphorus from non-organic phases, such as crystalline or inner-sphere complexed Al-bound phosphates that are not fully dissolved in previous extraction steps (Raiswell et al., 1994; Thompson et al., 2019). In Fe_I-2, the total P recovery was less than 70%, suggesting incomplete extraction and potential misassignment of refractory P phases (e.g., crystalline Al-P) as P_{org}. This is supported by the strong Al-P signal detected via ^{31}P NMR and XANES in this sample. Even if P_{org} is present, its detection via XANES is challenging due to similarity in the X-ray absorption near-edge structure of organic phosphorus and certain inorganic phosphates (e.g., phosphate adsorbed on clays or Al minerals). The white-line positions and post-edge features of organic P often overlap with those of inorganic phases, making unambiguous identification difficult without complementary techniques such as ^{31}P NMR or wet chemical analysis (Li et al., 2015; Negassa et al., 2010). Moreover, the low concentration of P_{org} relative to total P in most samples (except Fe_I-2) further diminishes its spectral contribution.

5.2. Evaluating potential transformation of P phases and lithological controls on P partitioning

Previous studies have shown that Late Devonian OIS deposits developed mostly at low to middle paleolatitudes (**Fig. 1A**), under conditions characterized by a warm and humid climate (Van Houten, 1985; Van Houten and Arthur, 1989). Growing evidence indicates a global expansion of deeply rooted vascular plants and a significant increase in terrestrial biomass in the Late Devonian (Algeo and Scheckler, 1998, 2010). The coeval uplift of the Acadian-Eovariscan orogenic belt increased the exposure of fresh rocks, thus increasing physical and chemical erosion (Averbuch et al., 2005). These processes collectively suggest intensified continental weathering during the Late Devonian, leading to elevated terrestrial fluxes of elements such as phosphorus and iron into the ocean (Baioumy et al., 2017; Burkhalter, 1995; Diab et al., 2020; Liu et al., 2017; Salama et al., 2014; Van Houten, 1985; Van Houten and Arthur, 1989). It is also noteworthy that a recent study of end-Devonian ironstones in South China proposes that a proportion of the Fe in these ironstones may have been sourced from hydrothermal venting in a redox-stratified ocean, with Fe^{2+} transported to shelves via storm-induced upwelling (Lyu et al., 2025). Nevertheless, our dataset reveals a strong positive correlation between total phosphorus and Fe contents in the OIS samples (R^2 = 0.81; **Fig. S2)**. This relationship is not observed in the interlayer samples, implying that Fe exerted a dominant primary control on P sequestration within the OIS samples.

The formation of oolitic ironstones may be strongly controlled by water depth (e.g., Hallam and Bradshaw, 1979; Young, 1989). This resulted in a two-stage formation of the Ningxiang ore deposit being proposed in a previous study (Gan et al., 2021), whereby dissolved Fe^{2+} accumulated under the more reducing conditions that prevailed during transgressive phases, and this Fe^{2+} was subsequently oxidized and deposited as Fe (oxyhydr)oxides in shallow, oxic waters during regressive phases, ultimately forming the oolitic ironstone layers. On the basis of the evolution of the sedimentary facies and fossil distributions, a broad scale sea level transgression is indicated through the studied interval (**Fig. 2B;** Gan et al., 2021). The minerals forming the ooids are generally tangentially arranged and concentrically distributed, indicating mobilization in the water column during formation (Baioumy et al., 2017; Diab et al., 2020; Rahiminejad and Zand-Moghadam, 2018). Specifically, the abundant detrital material, poor roundness of the quartz grains and concentric laminated structure indicate that the Huangjiadeng Formation was deposited in the littoral zone under strongly hydrodynamic conditions (**Figs. 4A, B**). The presence of minor brachiopod and echinoderm fossils, combined with the uniform distribution of ooids and their minimal evidence of abrasion or breakage **(Fig. 4I)**, all support an interpretation of deposition in a lower-energy, relatively deeper-water (i.e., more offshore) environment within the neritic zone of the Xiejingsi Formation.

Our Fe *K-edge* EXAFS analyses also suggest that iron oxides (dominantly hematite) are the major Fe minerals in all OIS samples, accounting for>80% of total

Fe (**Fig. 11C; Table S1**). In addition, vivianite tends to increase from Fe_I to Fe_{IV}, where it accounts for ~20% of the mineral phases in Fe_{IV}-1, while magnetite is more common (~13%) in Fe_I-1 and Fe_I-2 **(Fig. 11C; Table S1).** The predominant presence of iron oxides suggests that these OIS samples were most likely deposited under oxygenated bottom waters, while the appearance of vivianite in the upper formation indicates relatively more reducing conditions, that likely developed in pore waters.

Our S K-edge XANES results show a primary $CaSO_4$ composition for the Huangjiadeng samples (**Fig. 12; Table S1**), indicating deposition in an evaporitic setting, likely relating to marine regression (e.g., Warren, 2016). This is consistent with a shallow, nearshore setting that would have been prone to emersion and evaporation. The S *K-edge* XANES data show stratigraphic changes from dominant gypsum (evaporative conditions) in the lower formation, to an increased presence of pyrite (anoxic conditions) in the upper interlayers. This trend supports a long-term transgression that gradually led to more persistently submerged and potentially redox-stratified conditions, within which shorter-term regression-evaporation cycles occurred. Under periodic restriction and evaporative conditions during deposition of the Huangjiadeng Formation, thin OIS layers, such as Fe_I and Fe_{II}, formed because of less Fe^{2+} recycling to the oxic water column during sediment reworking (Gan et al., 2021; Liu et al., 2017). By contrast, the host rocks of Fe_{III} and Fe_{IV} in the Xiejingsi Formation are carbonates, and the ooids are intact (**Figs. 4C-I**). Many ostracods and a few brachiopods or echinoderms occur in these layers (**Figs. 4D, F and I**). Therefore, it is inferred that Fe_{III} and Fe_{IV} formed in the neritic zone under weaker hydrodynamic conditions. However, the multiple cycles of shale-limestone-sandstone-mudstone in the Xiejingsi Formation indicate shorter-timescale fluctuations in sea level during transgression events (**Fig. 2B**). Three sublayers of Fe_{III} formed during this period, which is consistent with the formation of OISs in discontinuous horizons caused by sea level fluctuation (Burkhalter, 1995).

This two-stage formation model for OISs provides a coherent explanation for the observed transition from Al/Fe-bound P in the Huangjiadeng Formation to Ca-bound P in the Xiejingsi Formation (**Figs. 6, 8-10**). In the first stage, the pronounced increase in pyrite content from the Huangjiadeng Formation to the Xiejingsi Formation (**Fig. 12C**; **Table S1**) indicates a more reducing diagenetic environment, likely associated with persistent anoxic porewaters near the sediment-water interface (e.g., Giblin and Howarth, 1984; Raiswell et al., 1993). Under such conditions, both Fe^{2+} and phosphate would have accumulated in the porewaters through organic matter degradation and the reductive dissolution of Fe (oxyhydr)oxides (Slomp et al., 1996; Ruttenberg and Berner, 1993). In the second stage, marine regression increased local hydrodynamic energy, promoting sediment resuspension and partial oxidation. When the hydrodynamic force weakened, Fe-P colloids and clay minerals adhered to the surface of the detritus (as the core of the ooids), forming ooids. In the presence of micromolar dissolved Ca^{2+} in porewaters, the accumulation of dissolved P led to the precipitation of calcium phosphate, mainly in the form of CFA (Ruttenberg and Berner, 1993; **Fig. 10**), giving the high proportions of Ca-P in the OIS samples from the Xiejingsi Formation.

The Al-P phases may have formed during phosphate diagenesis in these shallow-marine and shelf deposits, a process observed in ancient marine sandstones (Rasmussen, 1996; Ruttenberg, 2014), representing an underappreciated marine P sink. Alternatively, in-situ P uptake by clay minerals during continental weathering may also have contributed. Our ^{31}P solid-state NMR data support both possibilities. Sample Fe_I-1 shows a chemical shift near –11 ppm, consistent with detrital crystalline Al-phosphate (e.g., wavellite or variscite) derived from terrestrial weathering (Cade-Menun, 2005). By contrast, Fe_I-2 exhibits a less negative shift (~ –5 ppm), indicating a more labile, adsorbed form—likely an authigenic Al-P phase formed through inner-sphere complexation of phosphate with Al-OH groups on kaolinite or gibbsite surfaces during early diagenesis (Li et al., 2013; Van Emmerik et al., 2007).

5.3. Revisiting the application of the P/Fe proxy in iron-rich sediments

Having established the lithological control on P partitioning, we next examine its implications for the P/Fe proxy. Bjerrum and Canfield (2002) first proposed the use of P/Fe ratios in iron-rich sediments to reconstruct ancient marine phosphate concentrations, operating on the premise that phosphorus was primarily scavenged by Fe (oxyhydr)oxides. Subsequent laboratory studies refined this proxy by examining P adsorption onto iron oxides in silica-rich solutions (Konhauser et al., 2007; Planavsky et al., 2010), as well as in the presence of major seawater cations such as Ca^{2+} and Mg^{2+} (Jones et al., 2015). However, the reliability of this proxy depends on the preservation of the primary Fe-P relationship. Post-depositional transformations—including reductive dissolution of Fe (oxyhydr)oxides, re-adsorption of released phosphate, and re-precipitation as authigenic Ca-phosphates—can substantially modify bulk P/Fe ratios (Slomp et al., 1996; Ruttenberg, 2014; Schad et al., 2021). Consequently, deviations in P/Fe values may reflect diagenetic redistribution rather than primary seawater chemistry.

As demonstrated in Section 5.2, extensive diagenetic transformation from Fe- and Al-bound to Ca-bound phosphorus likely altered the primary Fe-P association in these OIS samples, raising concerns about the reliability of the P/Fe proxy when applied to Phanerozoic ironstones. To assess the extent of diagenetic modification, we compared bulk P_{tot}/Fe*100 values (e.g., Planavsky et al., 2010) with phase-specific P data. A strong correlation between P_{auth} (authigenic Ca-P) and P_{tot}/Fe*100 ($R^2 = 0.73$; **Fig. S3**) contrasts sharply with the weak relationship observed between bulk Ca and P_{tot}/Fe*100 ($R^2 = 0.10$; **Fig. S3**). This decoupling reflects the fact that the bulk Ca content is dominated by carbonate minerals (e.g., calcite cements and fossil shells) that are not major P hosts. By contrast, P_{auth} records the formation of authigenic Ca-P minerals that incorporate additional P released during Fe (oxyhydr)oxide transformations. This mechanism may explain why the Huangjiadeng (2.72) and Xiejingsi (5.07) formations yield markedly higher P_{tot}/Fe*100 values relative to coeval marine sediments (e.g., 0.39 in Planavsky et al., 2010; 0.70 in Leistel et al., 1998).

Our observations also reveal that Al-bearing minerals represent an additional, previously unaccounted for, P sink. Both crystalline Al-phosphates and adsorbed Al-P surface complexes contribute appreciably to the total P inventory, particularly in samples from the lower Huangjiadeng Formation. Such phases may originate from detrital input or in-situ authigenic precipitation, and their presence introduces further complexity into bulk P/Fe proxies because they decouple phosphorus accumulation from Fe (oxyhydr)oxide abundance. Collectively, these results demonstrate that diagenetic redistribution and multi-phase partitioning may impact P/Fe ratios in ironstone samples. Reliable reconstructions may thus benefit from additional insight afforded by phase-specific quantification of Fe and P hosts. Hence, application of the P/Fe proxy to Phanerozoic ironstones should be grounded in mineralogical and phase-specific constraints.

6. Conclusions

We integrated sequential extraction, ^{31}P solid-state NMR, and P *K-edge* XANES spectroscopy to quantitatively constrain phosphorus partitioning in Late Devonian oolitic ironstones. During diagenesis, primary Fe (oxyhydr)oxides were transformed into hematite and secondary clay minerals, releasing adsorbed phosphorus to porewaters. A substantial fraction of this mobilized P was subsequently retained as authigenic apatite or re-adsorbed onto residual Fe (oxyhydr)oxides. The redistribution of phosphorus phases, driven by variations in water depth, circulation and porewater redox conditions, exerts a first-order control on bulk P/Fe ratios. These variations complicate the use of P/Fe as a straightforward proxy for ancient seawater phosphate concentrations, when applied to Phanerozoic ironstones. Our results show that Fe-bound phosphorus is not necessarily dominant even in Fe-rich deposits, and that Al-bearing minerals can constitute an overlooked sink for sedimentary P. Integrating NMR and XANES with sequential extractions provides a quantitative, cross-validated framework for resolving P phase partitioning and for refiningpaleo-phosphate proxies in iron-rich sediments.

Data availability

Data are available through Mendeley Data at DOI: 10.17632/c9jtdd9ff5.2

Acknowledgements

We acknowledge the associate editor Prof. Chao Li for editorial handling of the manuscript and three anonymous reviewers for providing constructive comments on our manuscript. This research was funded by the National Natural Science Foundation of China (Grant No. 42421002). We also thank Prof. Xiumian Hu for insightful suggestions that helped improve the manuscript. JHH acknowledges the National Natural Science Foundation of China (42173083) and CIFAR Azrieli Global Scholars for financial support. We are also grateful to the Beijing Synchrotron Radiation Facility (BSRF, China) for assisting with the Fe *K-edge* EXAFS and S *K-edge* XANES data collection. The P *K-edge* XANES data were collected at beamline X15B at the National Synchrotron Light Source (NSLS), Brookhaven National Laboratory (Upton, NY), Soft X-ray Microcharacterization Beamline (SXRMB), and the Canadian Light Source (CLS). Research at the Canadian Light Source was supported by the Natural Sciences and Engineering Research Council of Canada, the National Research Council Canada, the Canadian

Institutes of Health Research, the Province of Saskatchewan Western Economic Diversification Canada, and the University of Saskatchewan.

References

Alcott, L.J., Mills, B.J.W., Bekker, A., Poulton, S.W., 2022. Earth's Great Oxidation Event facilitated by the rise of sedimentary phosphorus recycling. Nat. Geosci. 15, 210.

Algeo, T.J., Scheckler, S.E., 1998. Terrestrial-marine teleconnections in the Devonian: links between the evolution of land plants, weathering processes, and marine anoxic events. Philos. Trans. R. Soc. B-Biol. Sci. 353, 113-128.

Algeo, T.J., Scheckler, S.E., 2010. Land Plant Evolution and Weathering Rate Changes in the Devonian. J. Earth Sci. 21, 75-78.

Anderson, L.D., Delaney, M.L., Faul, K.L., 2001. Carbon to phosphorus ratios in sediments: Implications for nutrient cycling. Global Biogeochemical Cycles 15, 65-79.

Averbuch, O., Tribovillard, N., Devleeschouwer, X., Riquier, L., Mistiaen, B., van Vliet-Lanoe, B., 2005. Mountain building-enhanced continental weathering and organic carbon burial as major causes for climatic cooling at the Frasnian-Famennian boundary (c. 376 Ma)? Terr. Nova 17, 25-34.

Baioumy, H., Omran, M., Fabritius, T., 2017. Mineralogy, geochemistry and the origin of high-phosphorus oolitic iron ores of Aswan, Egypt. Ore Geol. Rev. 80, 185-199.

Bekker, A., Slack, J.F., Planavsky, N., Krapez, B., Hofmann, A., Konhauser, K.O., Rouxel, O.J., 2010. Iron Formation: The Sedimentary Product of a Complex Interplay among Mantle, Tectonic, Oceanic, and Biospheric Processes. Econ. Geol. 105, 467-508.

Bjerrum, C.J., Canfield, D.E., 2002. Ocean productivity before about 1.9 Gyr ago limited by phosphorus adsorption onto iron oxides. Nature 417, 159-162.

Brandes, J.A., Ingall, E., Paterson, D., 2007. Characterization of minerals and organic phosphorus species in marine sediments using soft X-ray fluorescence spectromicroscopy. Mar. Chem. 103, 250-265.

Burkhalter, R.M., 1995. Ooidal ironstones and ferruginous microbialites: origin and relation to sequence stratigraphy (Aalenian and Bajocian, Swiss Jura mountains). Sedimentology 42, 57-74.

Cade-Menun, B.J., 2005. Characterizing phosphorus in environmental and agricultural samples by 31P nuclear magnetic resonance spectroscopy. Talanta 66, 359-371.

Dam, T.T.N., Angert, A., Krom, M.D., Bigio, L., Hu, Y., Beyer, K.A., Mayol-Bracero, O.L., Santos-Figueroa, G., Pio, C. Zhu, M., 2021. X-ray spectroscopic quantification of phosphorus transformation in Saharan dust during trans-atlantic dust transport. Environ. Sci. Technol. 55, 12694-12703.

Defforey, D., Paytan, A., 2018. Phosphorus cycling in marine sediments: Advances and challenges. Chem. Geol. 477, 1-11.

Diab, H., Chouabbi, A., Chi Fru, E., Nacer, J.-E., Krekeler, M., 2020. Mechanism of formation, mineralogy and geochemistry of the ooidal ironstone of Djebel Had, northeast Algeria. J. African Earth Sci. 162.

Du, Y.S., Gong, Y.M., Liu, B.P., Feng, Q.L., Wu, Y., 1996. Devonian sequence stratigraphy and sea-level changes within the south china plate. Sedimentary Geology and Tethyan Geology 16, 14-23.

Follmi, K.B., 1996. The phosphorus cycle, phosphogenesis and marine phosphate-rich deposits. Earth Sci. Rev. 40, 55-124.

Gan, K., Wu, C., Yang, T., Liu, H., Ye, H., Xiang, M., Liu, J., Li, W., 2021. Characteristics and formation mechanism of ooidal ironstones: indicating from the Huoshaoping iron deposit, Western Hubei Province, China. Acta Geologica Sinica 95(08), 2493-2508.

Giblin, A.E., Howarth, R.W., 1984. Porewater evidence for a dynamic sedimentary iron cycle in salt marshes. Limnol. Oceanogr. 29, 47-63

Giguet-Covex, C., Poulenard, J., Chalmin, E., Arnaud, F., Rivard, C., Jenny, J.P., Dorioz, J.M., 2013. XANES spectroscopy as a tool to trace phosphorus transformation during soil genesis and mountain ecosystem development from lake sediments. Geochim. Cosmochim. Acta 118, 129-147.

Golonka, J., 2011. Chapter 6 Phanerozoic palaeoenvironment and palaeolithofacies maps of the Arctic region. Geological Society, London, Memoirs 35, 79-129.

Guilbaud, R., Poulton, S.W., Thompson, J., Husband, K.F., Zhu, M.Y., Zhou, Y., Shields, G.A., Lenton, T.M., 2020. Phosphorus-limited conditions in the early Neoproterozoic ocean maintained low levels of atmospheric oxygen. Nat. Geosci. 13, 296.

Hallam, A., Bradshaw, M. J., 1979. Bituminous shales and oolitic ironstones as indicators of transgressions and regressions. Journal of the Geological Society, 136(2), 157-164.

Iacumin, P., Bocherens, H., Mariotti, A., Longinelli, A., 1996. Oxygen isotope analyses of co-existing carbonate and phosphate in biogenic apatite: A way to monitor diagenetic alteration of bone phosphate? Earth Planet. Sci. Lett. 142, 1-6.

Ingall, E.D., Bustin, R.M., Vancappellen, P., 1993. Influence of water column anoxia on the burial and preservation of carbon and phosphorus in marine shales. Geochim. Cosmochim. Acta 57, 303-316.

Ingall, E., Jahnke, R., 1994. Evidence for enhanced phosphorus regeneration from marine sediments overlain by oxygen depleted waters. Geochim. Cosmochim.

Acta 58, 2571-2575.

Ingall, E., Jahnke, R., 1997. Influence of water-column anoxia on the elemental fractionation of carbon and phosphorus during sediment diagenesis. Mar. Geol. 139, 219-229.

Jilbert, T., Slomp, C.P., 2013. Iron and manganese shuttles control the formation of authigenic phosphorus minerals in the euxinic basins of the Baltic Sea. Geochim. Cosmochim. Acta 107, 155-169.

Johnson, B.B., Ivanov, A.V., Antzutkin, O.N., Forsling, W., 2002. P-31 nuclear magnetic resonance study of the adsorption of phosphate and phenyl phosphates on gamma-Al2O3. Langmuir 18, 1104-1111.

Jones, C., Nomosatryo, S., Crowe, S.A., Bjerrum, C.J., Canfield, D.E., 2015. Iron oxides, divalent cations, silica, and the early earth phosphorus crisis. Geology 43, 135-138.

Kar, G., Hundal, L.S., Schoenau, J.J., Peak, D., 2011. Direct Chemical Speciation of P in Sequential Chemical Extraction Residues Using P *K-Edge* X-Ray Absorption Near-Edge Structure Spectroscopy. Soil Sci. 176, 589-595.

Kizewski, F., Liu, Y.T., Morris, A., Hesterberg, D., 2011. Spectroscopic Approaches for Phosphorus speciation in soils and other environmental systems. J. Environ. Qual. 40, 751-766.

Konhauser, K.O., Lalonde, S.V., Amskold, L., Holland, H.D., 2007. Was there really an

Archean phosphate crisis? Science 315, 1234-1234.

Leistel, J.M., Marcoux, E., Deschamps, Y., 1998. Chert in the Iberian Pyrite Belt. Miner. Depos. 33, 59-81.

Li, W., Feng, J., Kwon, K.D., Kubicki, J.D., Phillips, B.L., 2010. Surface speciation of phosphate on boehmite (γ-AlOOH) determined from NMR spectroscopy. Langmuir 26, 4753-4761.

Li, W., Joshi, S.R., Hou, G., Burdige, D.J., Sparks, D.L., Jaisi, D.P., 2015. Characterizing phosphorus speciation of Chesapeake Bay sediments using chemical extraction, ^{31}P NMR, and X-ray absorption fine structure spectroscopy. Environ. Sci. Technol. 49, 203-211.

Li, W., Pierre-Louis, A.-M., Kwon, K.D., Kubicki, J.D., Strongin, D.R., Phillips, B.L., 2013. Molecular level investigations of phosphate sorption on corundum (α-Al_2O_3) by ^{31}P solid state NMR, ATR-FTIR and quantum chemical calculation. Geochim. Cosmochim. Acta 107, 252-266.

Li, W., Xu, W., Parise, J.B., Phillips, B.L., 2012. Formation of hydroxylapatite from co-sorption of phosphate and calcium by boehmite. Geochim. Cosmochim. Acta 85, 289-301.

Liu, J., Hu, Y.F., Yang, J.J., Abdi, D., Cade-Menun, B.J., 2015. Investigation of Soil Legacy Phosphorus Transformation in Long-Term Agricultural Fields Using Sequential Fractionation, P *K-edge* XANES and Solution P NMR Spectroscopy.

Environ. Sci. Technol. 49, 168-176.

Liu, Y., He, A., Yuankui, Q., Yang, H., Wu, Y., Si, X., Yao, J., Cheng, J., Zhang, H., Xu, Y., Wan, C., Chneg, L., Li, X., 2017. Zhongguo Ningxingshi Tiekuang. Metallurgical Industry Press, Beijing.

Lookman, R., Grobet, P., Merckx, R., Vlassak, K., 1994. Phosphate sorption by synthetic amorphous aluminum hydroxides - A Al-27 and P-31 solid-state MAS NMR spectroscopy study. Eur. J. Soil Sci. 45, 37-44.

Lyu, Y.J., Zhou, M.F., Cui, Y., Hu, R.Z., Liu, Z.R., Li, X.Y., 2025. Decoding the end-Devonian Hangenberg oceanic anoxia event: Insights from ironstones in South China. Earth Planet. Sci. Lett. 653, 11.

Ma, X.P., Zong, P., 2010. Middle and Late Devonian brachiopod assemblages, sea level change and paleogeography of Hunan, China. Sci. China-Earth Sci. 53, 1849-1863.

Mason, H.E., Montagna, P., Kubista, L., Taviani, M., McCulloch, M., Phillips, B.L., 2011. Phosphate defects and apatite inclusions in coral skeletal aragonite revealed by solid-state NMR spectroscopy. Geochim. Cosmochim. Acta 75, 7446-7457.

Matheson, E.J., Pufahl, P.K., 2021. Clinton ironstone revisited and implications for Silurian Earth system evolution. Earth-Sci. Rev. 215, 35.

McLennan, S.M., 2001. Relationships between the trace element composition of sedimentary rocks and upper continental crust. Geochem. Geophys. Geosyst. 2, 24.

Murphy, J., Riley, J.P., 1962. A modified single solution method for the determination of phosphate in natural waters. Anal. Chim. Acta 26, 31-&.

Negassa, W., Kruse, J., Michalik, D., Appathurai, N., Zuin, L., Leinweber, P., 2010. Phosphorus Speciation in Agro-Industrial Byproducts: Sequential Fractionation, Solution ^{31}P NMR, and P *K*- and $L_{2,3}$-Edge XANES Spectroscopy. Environ. Sci. Technol. 44, 2092-2097.

Paytan, A., McLaughlin, K., 2007. The oceanic phosphorus cycle. Chem. Rev. 107, 563-576.

Planavsky, N.J., Rouxel, O.J., Bekker, A., Lalonde, S.V., Konhauser, K.O., Reinhard, C.T., Lyons, T.W., 2010. The evolution of the marine phosphate reservoir. Nature 467, 1088-1090.

Poulton, S.W., Canfield, D.E., 2006. Co-diagenesis of iron and phosphorus in hydrothermal sediments from the southern East Pacific Rise: Implications for the evaluation of paleoseawater phosphate concentrations. Geochim. Cosmochim. Acta 70, 5883-5898.

Prietzel, J., Duemig, A., Wu, Y., Zhou, J., Klysubun, W., 2013. Synchrotron-based P *K-edge* XANES spectroscopy reveals rapid changes of phosphorus speciation in the topsoil of two glacier foreland chronosequences. Geochim.

Cosmochim. Acta 108, 154-171.

Pufahl, P.K., Grimm, K.A., 2003. Coated phosphate grains: Proxy for physical, chemical, and ecological changes in seawater. Geology 31, 801-804.

Qie, W., Ma, X., Xu, H., Qiao, L., Liang, K., Guo, W., Song, J., Chen, B., Lu, J., 2018. Devonian integrative stratigraphy and timescale of China. Sci. China Earth Sci. 62, 112-134.

Qiu, Z., Zou, C.N., Mills, B.J.W., Xiong, Y.J., Tao, H.F., Lu, B., Liu, H.L., Xiao, W.J., Poulton, S.W., 2022. A nutrient control on expanded anoxia and global cooling during the Late Ordovician mass extinction. Commun. Earth Environ. 3, 9.

Raiswell, R., Whaler, K., Dean, S., Coleman, M.L., Briggs, D.E.G., 1993. A simple three-dimensional model of diffusion-with-precipitation applied to localised pyrite formation in framboids, fossils and detrital iron minerals. Mar. Geol. 113, 89-100.

Raiswell, R., Canfield, D.E., Berner, R.A., 1994. A comparison of iron extraction methods for the determination of degree of pyritisation and the recognition of iron-limited pyrite formation. Chem. Geol. 111, 101-110.

Rahiminejad, A.H., Zand-Moghadam, H., 2018. Synsedimentary formation of ooidal ironstone: An example from the Jurassic deposits of SE central Iran. Ore Geol. Rev. 95, 238-257.

Rasmussen, B., 1996. Early-diagenetic REE-phosphate minerals (florencite, gorceixite, crandallite, and xenotime) in marine sandstones: A major sink for oceanic phosphorus. Am. J. Sci. 296, 601-632.

Ravel, B., Newville, M., 2005. ATHENA, ARTEMIS, HEPHAESTUS: data analysis for X-ray absorption spectroscopy using IFEFFIT. J. Synchrot. Radiat. 12, 537-541.

Reinhard, C.T., Planavsky, N.J., Gill, B.C., Ozaki, K., Robbins, L.J., Lyons, T.W., Fischer, W.W., Wang, C., Cole, D.B., Konhauser, K.O., 2017. Evolution of the global phosphorus cycle. Nature 541, 386-389.

Ruttenberg, K.C., 1992. Development of a sequential extraction method for different forms of phosphorus in marine-sediments. Limnol. Oceanogr. 37, 1460-1482.

Ruttenberg, K.C., 2014. The Global Phosphorus Cycle, in: Holland, H. D., Turekian, K. K. (Eds.), Treatise on Geochemistry. Elsevier, pp. 499-558.

Ruttenberg, K.C., Berner, R.A., 1993. Authigenic apatite formation and burial in sediments from non-upwelling, continental margin environments. Geochim. Cosmochim. Acta 57, 991-1007.

Salama, W., El Aref, M., Gaupp, R., Pufahl, P., 2014. Facies analysis and palaeoclimatic significance of ironstones formed during the Eocene greenhouse. Sedimentology 61, 1594-1624.

Schad, M., Halama, M., Jakus, N., Robbins, L.J., Warchola, T.J., Tejada, J., Kirchhof, R., Lalonde, S.V., Swanner, E.D., Planavsky, N.J., Thorwarth, H., Mansor, M., Konhauser, K.O., Kappler, A., 2021. Phosphate remobilization from banded iron formations during metamorphic mineral transformations. Chem. Geol. 584, 120489.

Schobben, M., Foster, W.J., Sleveland, A.R.N., Zuchuat, V., Svensen, H.H., Planke, S., Bond, D.P.G., Marcelis, F., Newton, R.J., Wignall, P.B., Poulton, S.W., 2020. A nutrient control on marine anoxia during the end-Permian mass extinction. Nat. Geosci. 13, 640.

Slomp, C.P., Epping, E.H.G., Helder, W., VanRaaphorst, W., 1996. A key role for iron-bound phosphorus in authigenic apatite formation in North Atlantic continental platform sediments. J. Mar. Res. 54, 1179-1205.

Slomp, C.P., Thomson, J., de Lange, G.J., 2002. Enhanced regeneration of phosphorus during formation of the most recent eastern Mediterranean sapropel (S1). Geochim. Cosmochim. Acta 66, 1171-1184.

Slomp, C.P., Thomson, J., de Lange, G.J., 2004. Controls on phosphorus regeneration and burial during formation of eastern Mediterranean sapropels. Mar. Geol. 203, 141-159.

Song, Y.F., Bowyer, F.T., Mills, B.J.W., Merdith, A.S., Wignall, P.B., Peakall, J., Zhang, S.C., Wang, X.M., Wang, H.J., Canfield, D.E., Shields, G.A., Poulton, S.W., 2023. Dynamic redox and nutrient cycling response to climate forcing in the

Mesoproterozoic ocean. Nat. Commun. 14, 10.

Thompson, J., Poulton, S.W., Guilbaud, R., Doyle, K.A., Reid, S., Krom, M.D., 2019. Development of a modified SEDEX phosphorus speciation method for ancient rocks and modern iron-rich sediments. Chem. Geol. 524, 383-393.

Tyrrell, T., 1999. The relative influences of nitrogen and phosphorus on oceanic primary production. Nature 400, 525-531.

Van cappellen, P., Ingall, E.D., 1994. Benthic phosphorus regeneration, net primaty production, and ocean anoxia — A model of the coupled marine biogeochemical cycles of carbon and phosphorus. Paleoceanography 9, 677-692.

Van Emmerik, T.J., Sandstrom, D.E., Antzutkin, O.N., Angove, M.J., Johnson, B.B., 2007. P-31 solid-state nuclear magnetic resonance study of the sorption of phosphate onto gibbsite and kaolinite. Langmuir 23, 3205-3213.

Van Houten, F.B., 1985. Oolitic ironstones and contrasting Ordovician and Jurassic paleogeography. Geology 13, 722-724.

Van Houten, F.B., Arthur, M.A., 1989. Temporal patterns among Phanerozoic oolitic ironstones and oceanic anoxia. Geological Soc Publishing House, Bath.

Warren, J.K., 2016. Evaporites: A geological compendium. Springer.

Westheimer, F.H., 1987. Why nature chose phosphates. Science 235, 1173-1178.

Xiong, Y., Guilbaud, R., Peacock, C.L., Cox, R.P., Canfield, D.E., Krom, M.D., Poulton, S.W., 2019. Phosphorus cycling in Lake Cadagno, Switzerland: A low sulfate euxinic ocean analogue. Geochim. Cosmochim. Acta 251, 116-135.

Yang, X.D., Xie, B.Q., Wang, L.J., Qin, Y.L., Henneman, Z.J., Nancollas, G.H., 2011. Influence of magnesium ions and amino acids on the nucleation and growth of hydroxyapatite. Crystengcomm 13, 1153-1158.

Yang, X.Q., Mao, J.W., Bowyer, F.T., Wu, C.Z., Li, R.X., Zhao, C., Yang, G.W., Poulton, S.W., 2024. A phosphate-rich marine reservoir in the redox stratified Ediacaran ocean. Commun. Earth Environ. 5, 8.

Young, T. P.,1989. Phanerozoic ironstones: an introduction and review. Geological Society, London, Special Publications, 46(1), 9-25.

Zhao, M., Zhang, S., Tarhan, L.G., Reinhard, C.T., Planavsky, N., 2020. The role of calcium in regulating marine phosphorus burial and atmospheric oxygenation. Nat. Commun. 11, 2232.

Zhou, M.F., Lyu, Y.J., Liu, Z.R., Liu, P.P., Meng, L., Qiu, W.J., Zhao, W.W., 2024. Devonian stratiform ironstone deposits in South China formed in a shallow marine environment of a passive continental margin. J. Asian Earth Sci. 262, 20.

Zhou, J. Y., Zheng, R. C., Zhang, Y. S., Zhu, Z. M., Li, X. Y., Luo, L. P., Zhou, M. G., 2009. Constraints of South China Devonian Ningxiang Palaeogeography on the Temporal and Spatial Distribution of Iron Ore Deposits and Their

Characteristics. Geological Science and Techology Information 28, 93-98.

Zhu, W., 2021. Sedimentary characteristics and metallogenic mechanism of Ningxiang-type iron deposits in South China. Sedimentary Geology and Tethyan Geology 43, 87-100.

Figures and tables

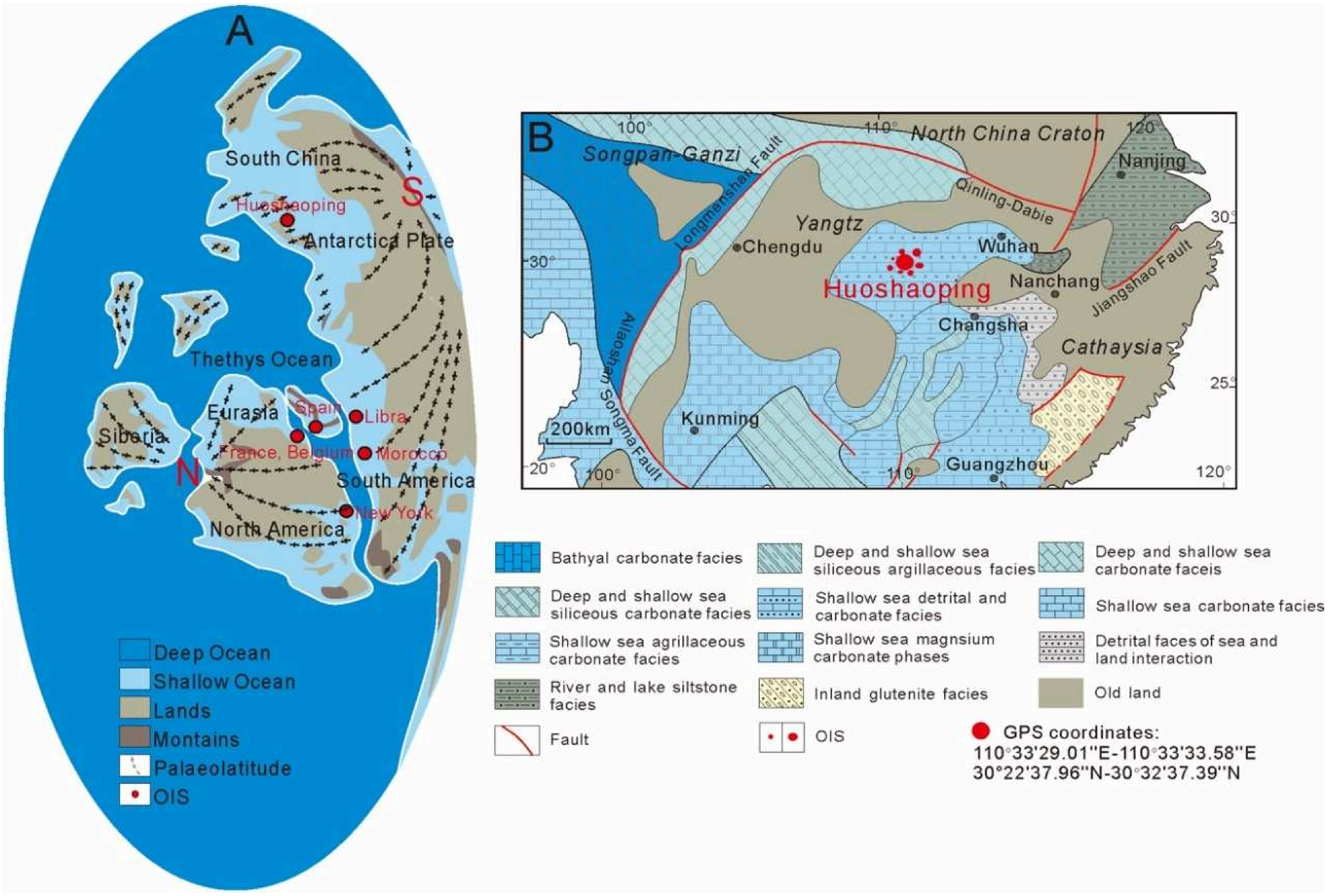

Fig. 1. Global distribution of oolitic ironstones (OISs) in the Late Devonian. A. Continental distribution modified from Golonka (2011) and Gan et al. (2021), and OIS distribution after Van Houten and Arthur (1989); B. Paleogeography and location of the Huoshaoping OIS in South China (modified from Zhou et al., 2009).

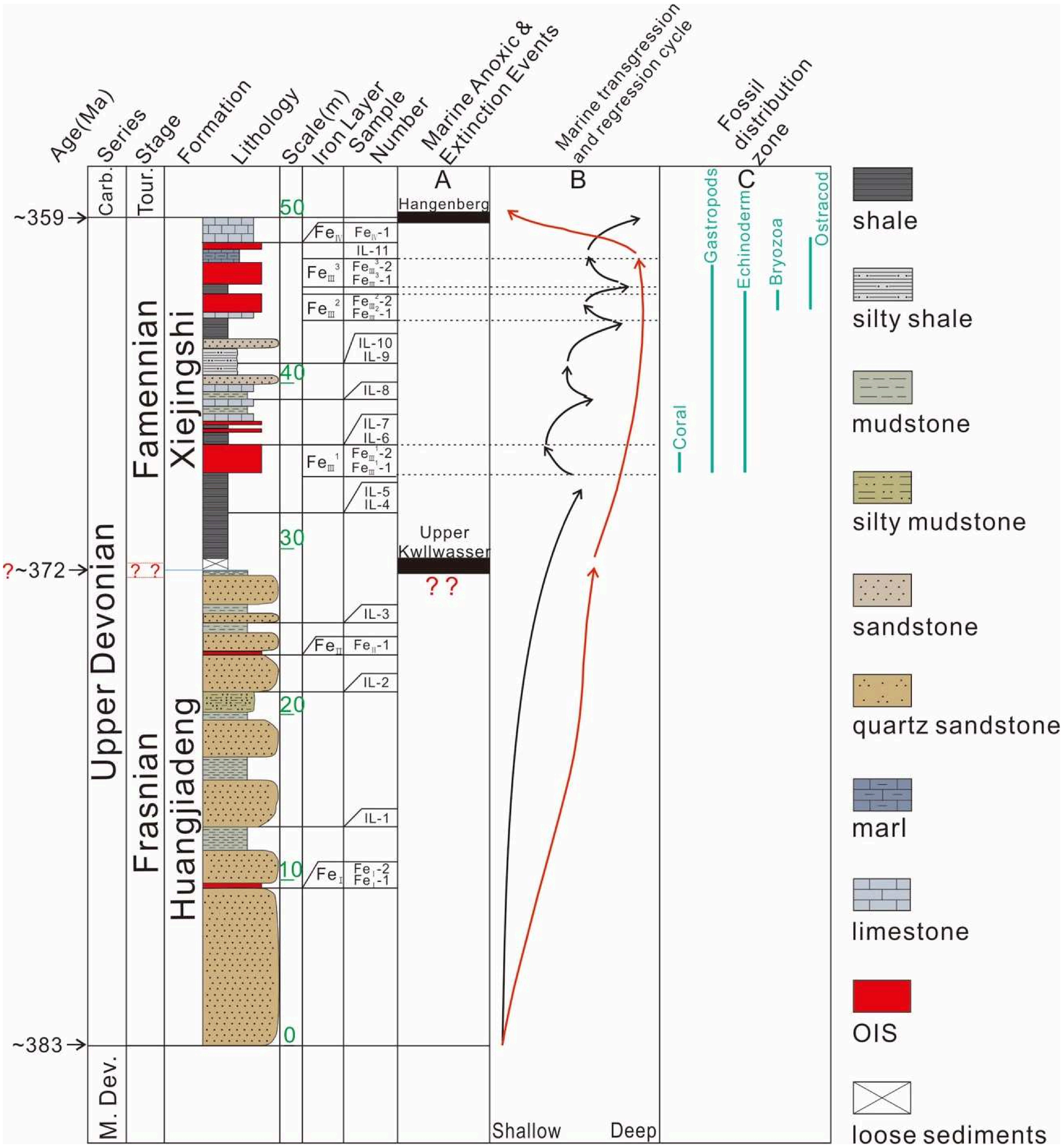

Fig. 2. Late Devonian global records. The stratigraphic framework was established according to Qie et al. (2018). A. Marine anoxic/extinction horizons (Algeo and Scheckler, 1998); B. Sea level change. Red line is from Liu et al. (2017), and the black line was established by sediment grain size (Du et al., 1996; Gan et al., 2021);

C. Fossil distribution zones (Gan et al., 2021). Question marks refer to uncertainty in the exact position of the boundary between the Frasnian and Famennian.

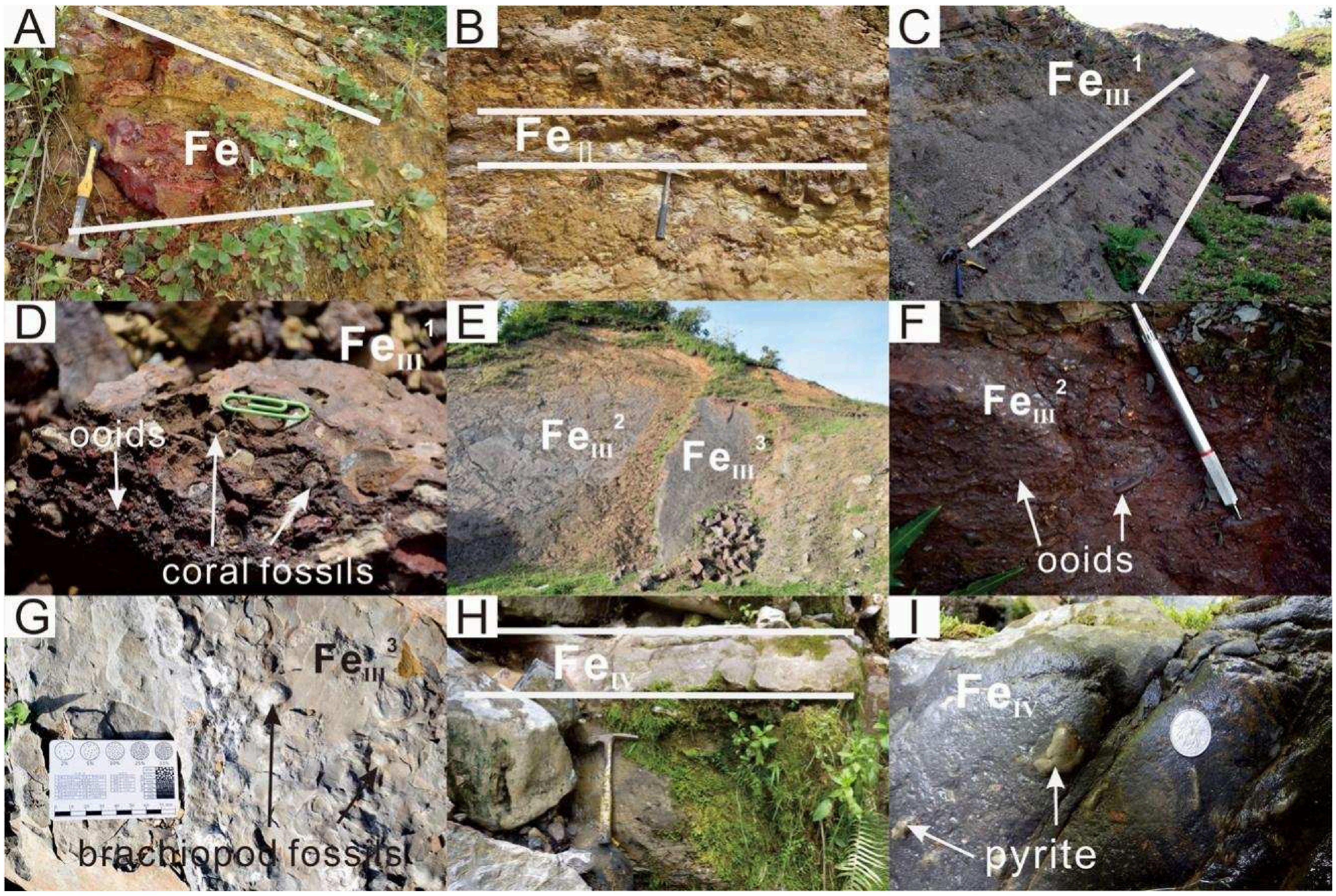

Fig. 3. Typical strata of the Huoshaoping iron formations. A. Fe_I in the Huangjiadeng Formation; B. Fe_{II} in the Huangjiadeng Formation; C. Fe_{III}^1 in the Xiejingsi Formation; D. Abundant ooids and coral fossils in Fe_{III}^1; E. Fe_{III}^2 and Fe_{III}^3 in the Xiejingsi Formation; F. Abundant iron ooids in Fe_{III}^2; G. Abundant brachiopod fossils in Fe_{III}^3; H. Fe_{IV} in the Xiejingsi Formation; I. Pyrite in Fe_{IV}.

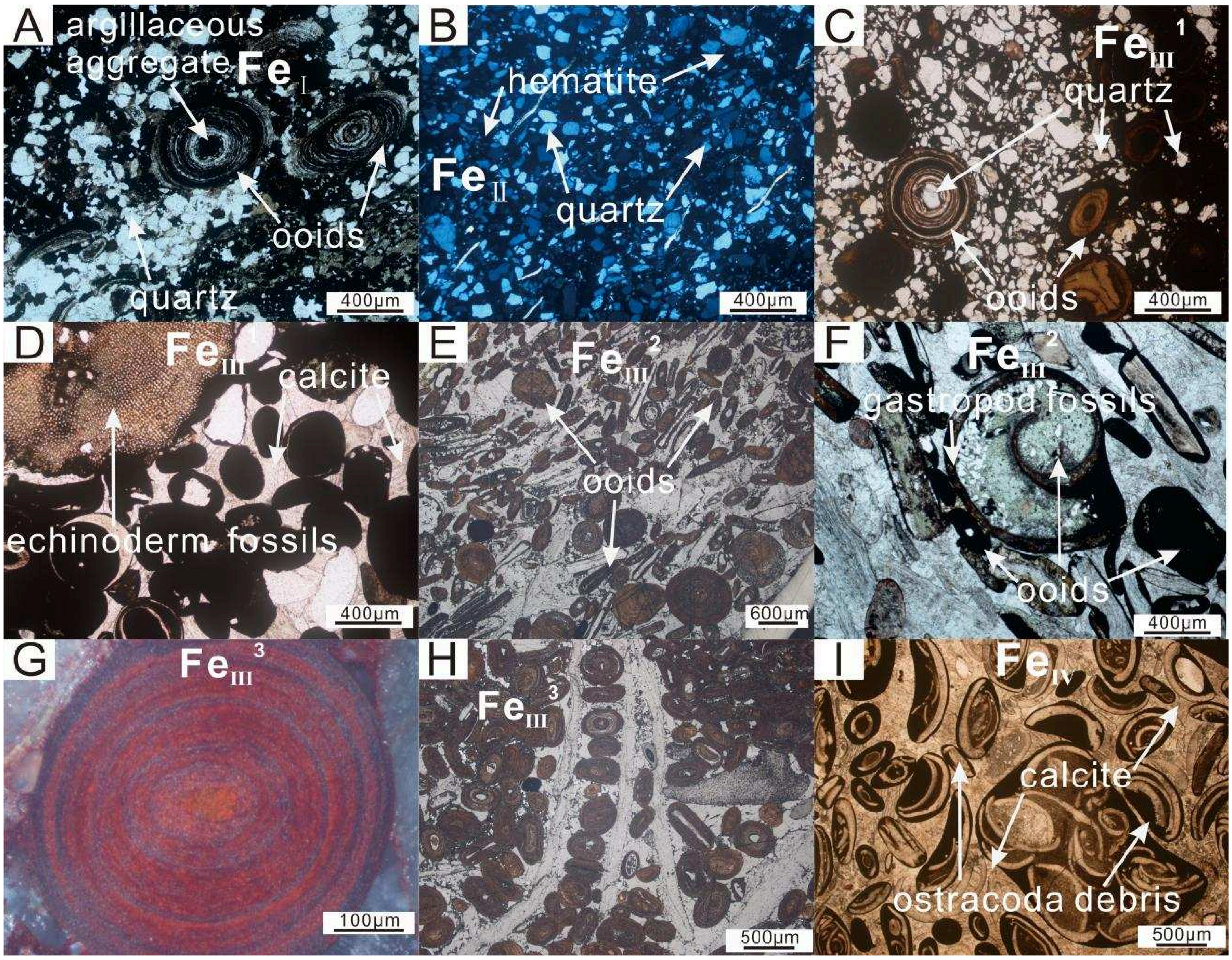

Fig. 4. Photomicrographs of ooids in the Huoshaoping iron formations. A. Iron ooids cemented by detrital quartz grains in Fe_I (transmittance plane-polarized light); B. No iron ooids were found in the Fe_{II} iron-bearing sandstones, and hematite (dark colour) was colloidal in cemented quartz (transmittance cross-polarized light); C. Iron ooids among quartz grains in Fe_{III}^1 (transmittance plane-polarized light); D. Echinoderm fossils and calcite cement in Fe_{III}^1 (transmittance plane-polarized light); E. High density of iron ooids in Fe_{III}^2, with diverse compositions and shapes (reflected light); F. Gastropod fossils and iron ooids in Fe_{III}^2, where some iron ooid clasts were found in the gastropod body cavity

(transmittance plane-polarized light); G. Iron ooid in Fe_{III}^3 (transmittance cross-polarized light); H. Fossil debris in Fe_{III}^3, with a high density of iron ooids (reflected light); I. Iron ooids cemented by calcite in Fe_{IV}, with the nuclei composed of ostracoda bioclasts, and laminae are thin (transmittance plane-polarized light).

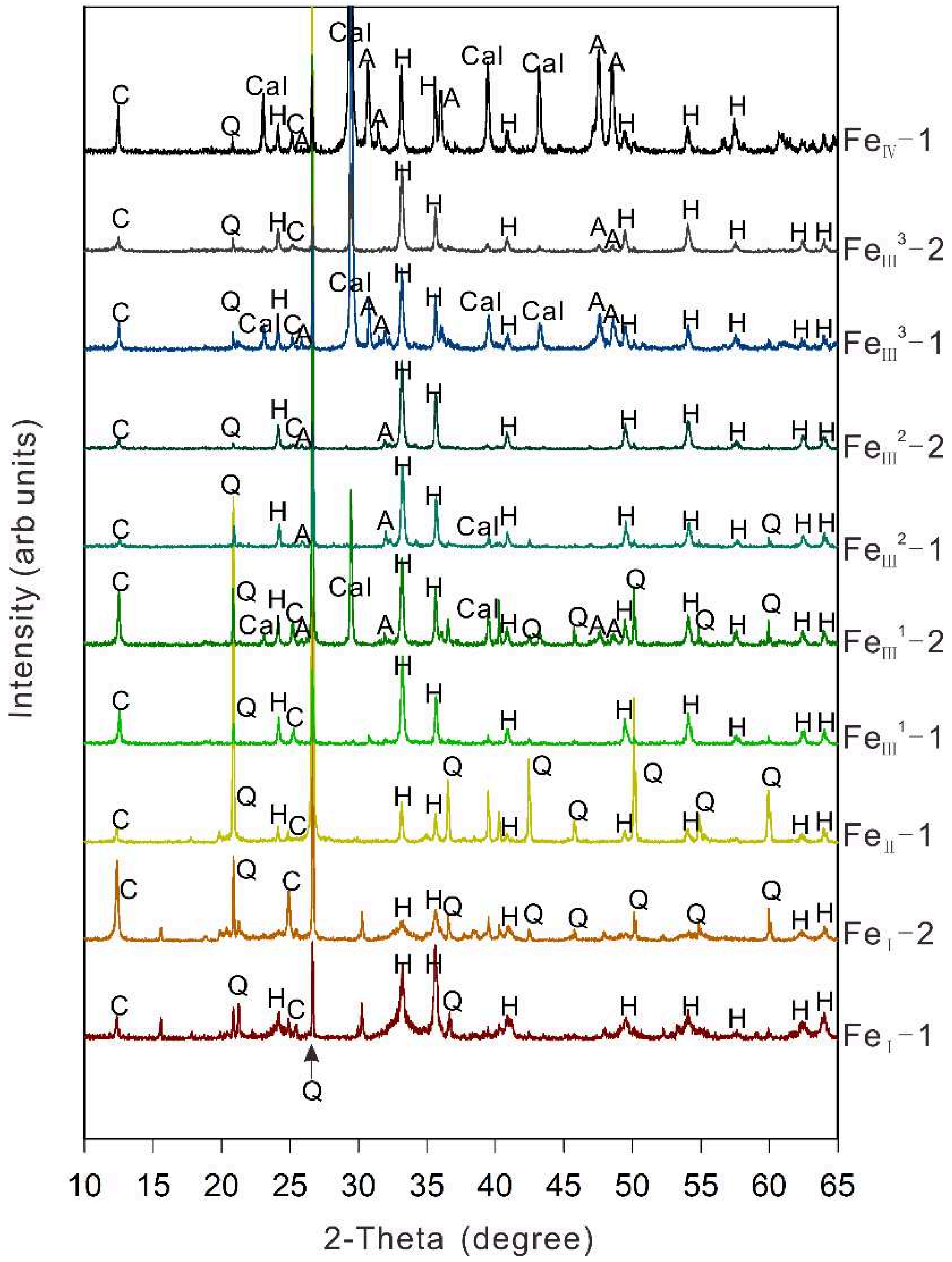

Fig. 5. X-ray diffraction patterns of the OIS samples. C: Chamosite ($(Fe,Mg)_3(Fe,Fe)_3[AlSi_3O_{10}](OH)_3$); H: Hematite ($Fe_2O_3$); Q: Quartz ($SiO_2$); A: Apatite ($Ca_5(PO_4)_3(F,Cl,OH)$); Cal: Calcite ($CaCO_3$).

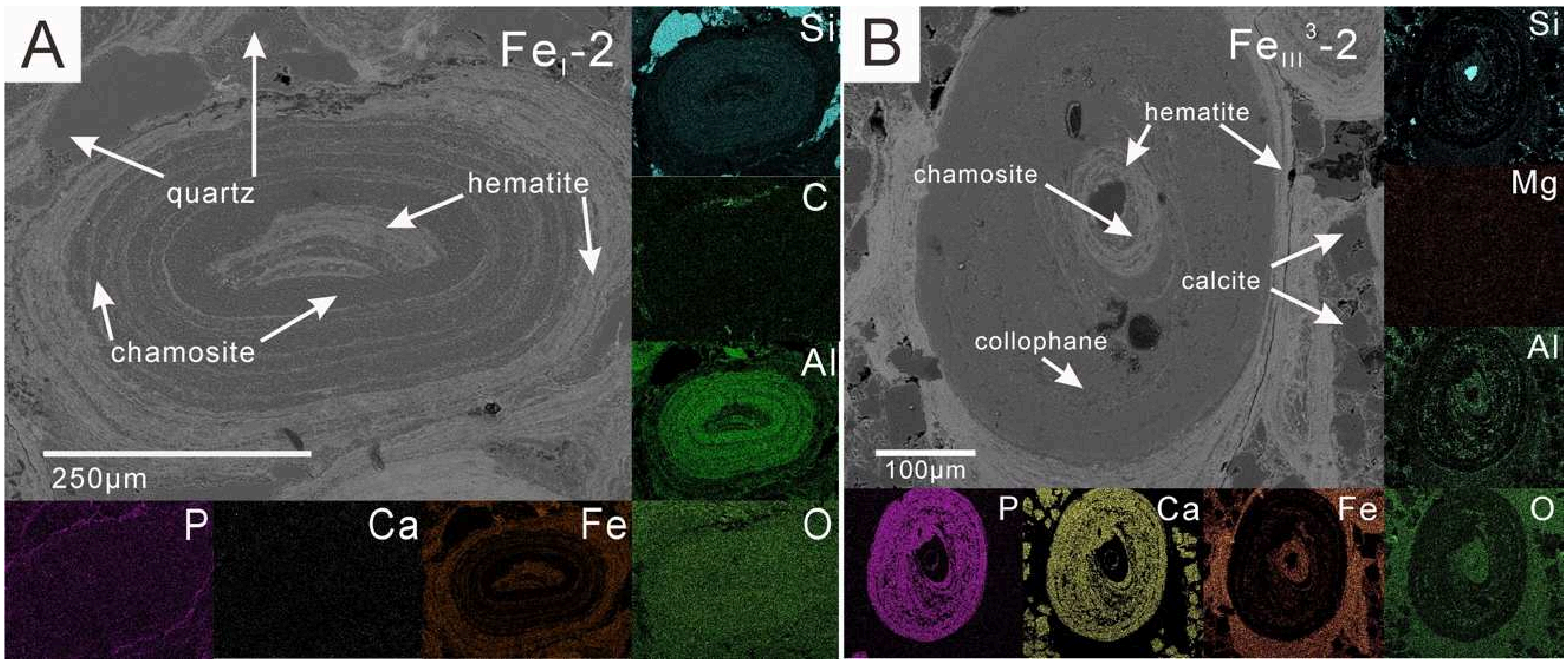

Fig. 6. SEM-EDS mapping images of iron ooids from Fe$_I$ (A) and Fe$_{III}$ (B). P and Fe have similar distribution patterns in Fe$_I$-2, whereas P and Ca have similar distribution patterns in Fe$_{III}$^{3}-2.

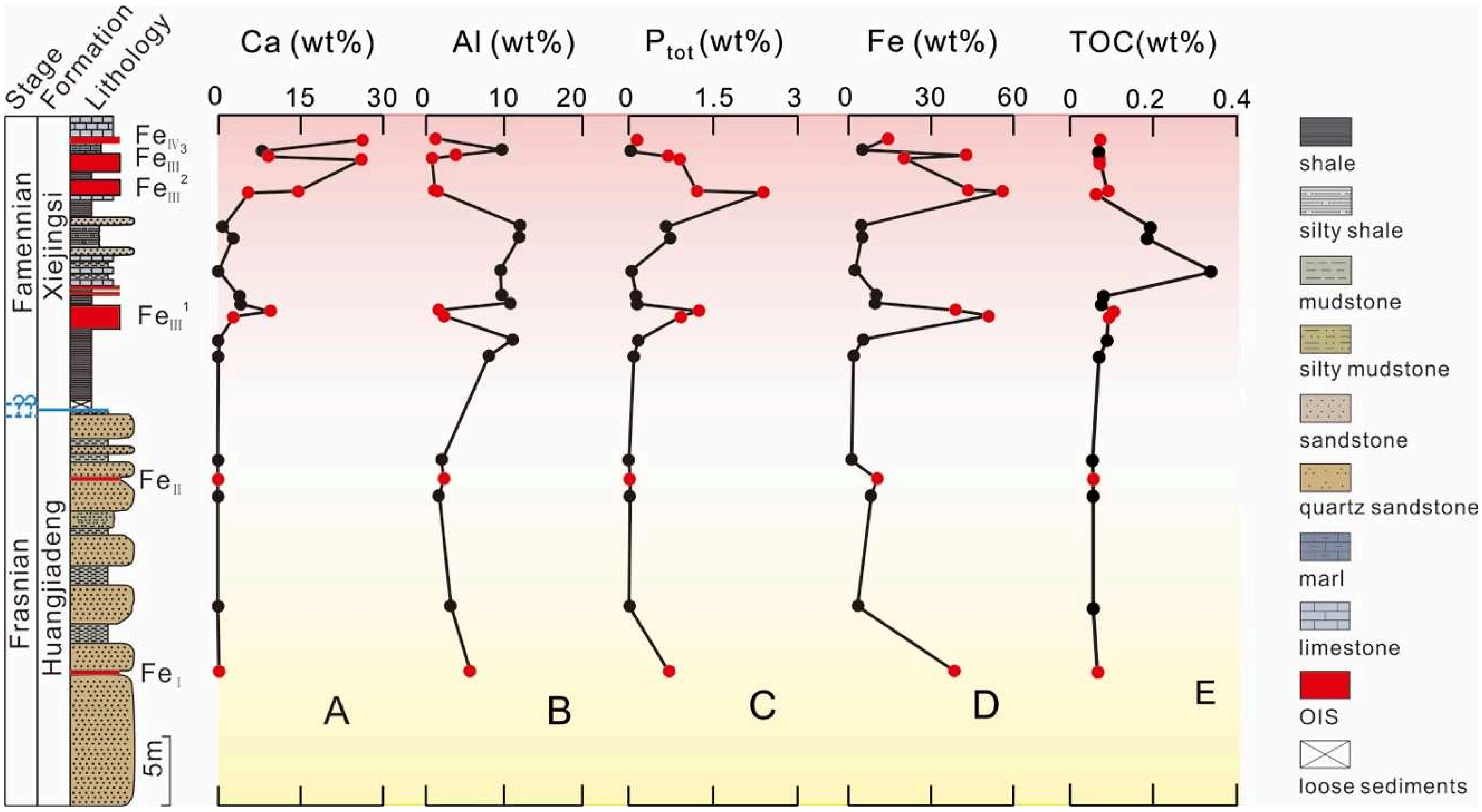

Fig. 7. Chemostratigraphic plots of major elements and TOC contents. P_{tot} represents total phosphorus content analysed after bulk sample digestion. Red datapoints represent ironstones.

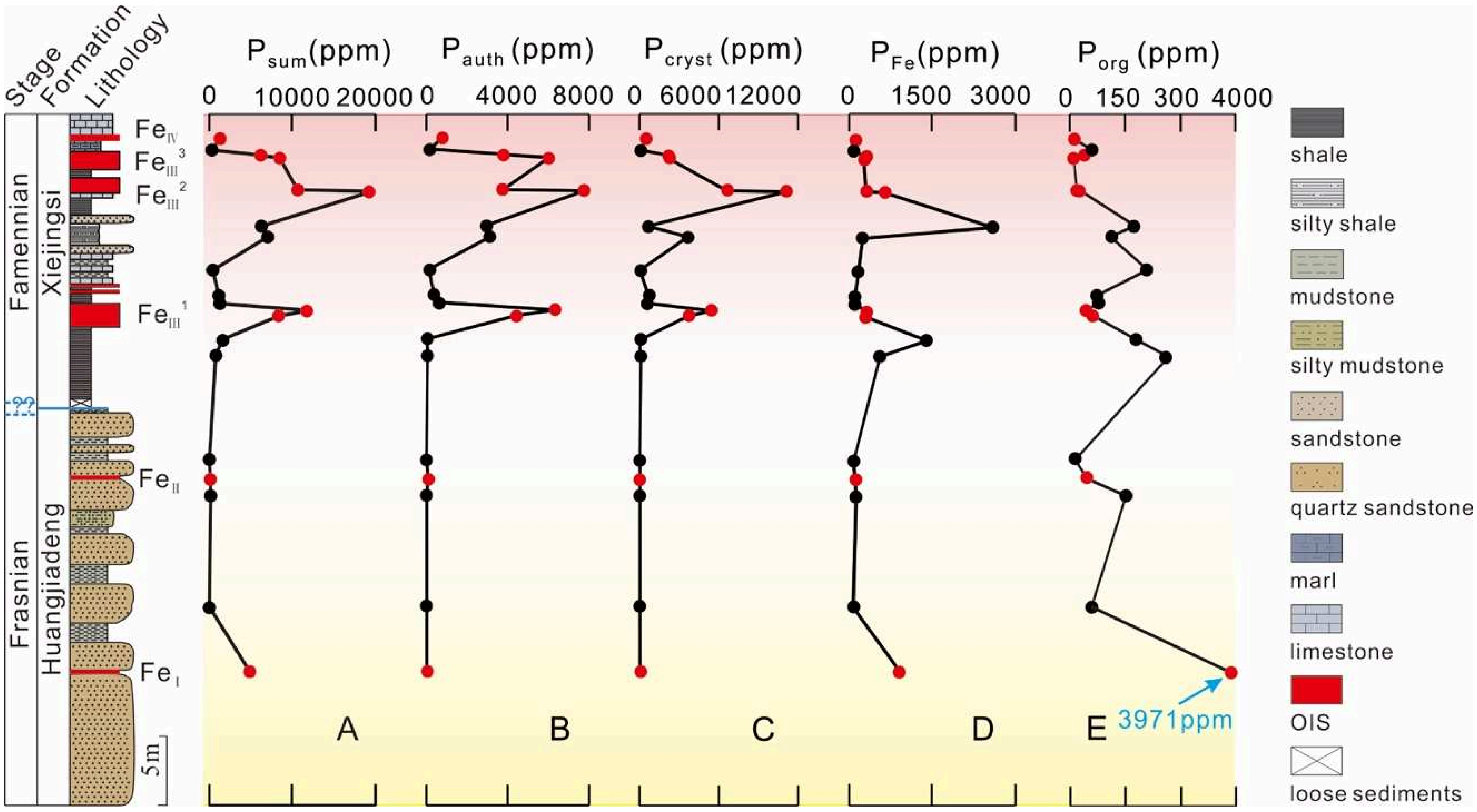

Fig. 8. Chemostratigraphic plots of P phases generated via sequential extraction. A. P_{sum} content (P_{sum} represents the sum of phosphorus contents analysed via sequential extraction); B. Authigenic P, comprising authigenic CFA, $CaCO_3$-bound P and biogenic apatite; C. Crystalline P, including detrital P and some crystalline P from the transformation of authigenic P; D. Iron-bound P, including iron oxide bound P, crystalline Fe bound P, and magnetite P; E. Organic P (data for Fe_I are excluded due to the very high P_{org} content in Fe_I).

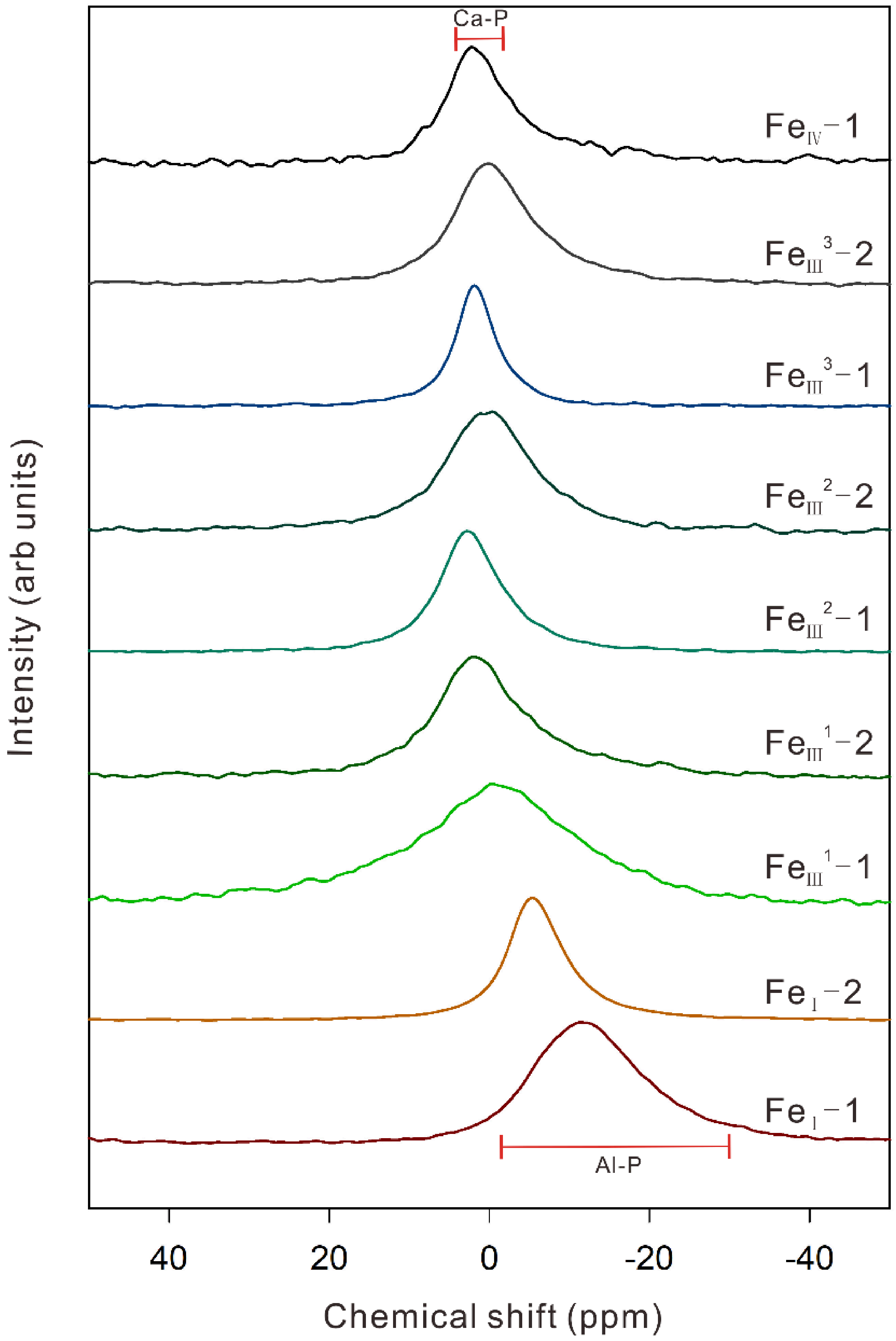

Fig. 9. ^{31}P solid-state NMR spectra of the OIS samples. Peaks ranging from -2 to 3 ppm are indicative of Ca-P minerals. Peaks ranging from -30 to -2 ppm are indicative of Al-P minerals. There was no NMR signal for Fe_{II} -1 because of its low P content.

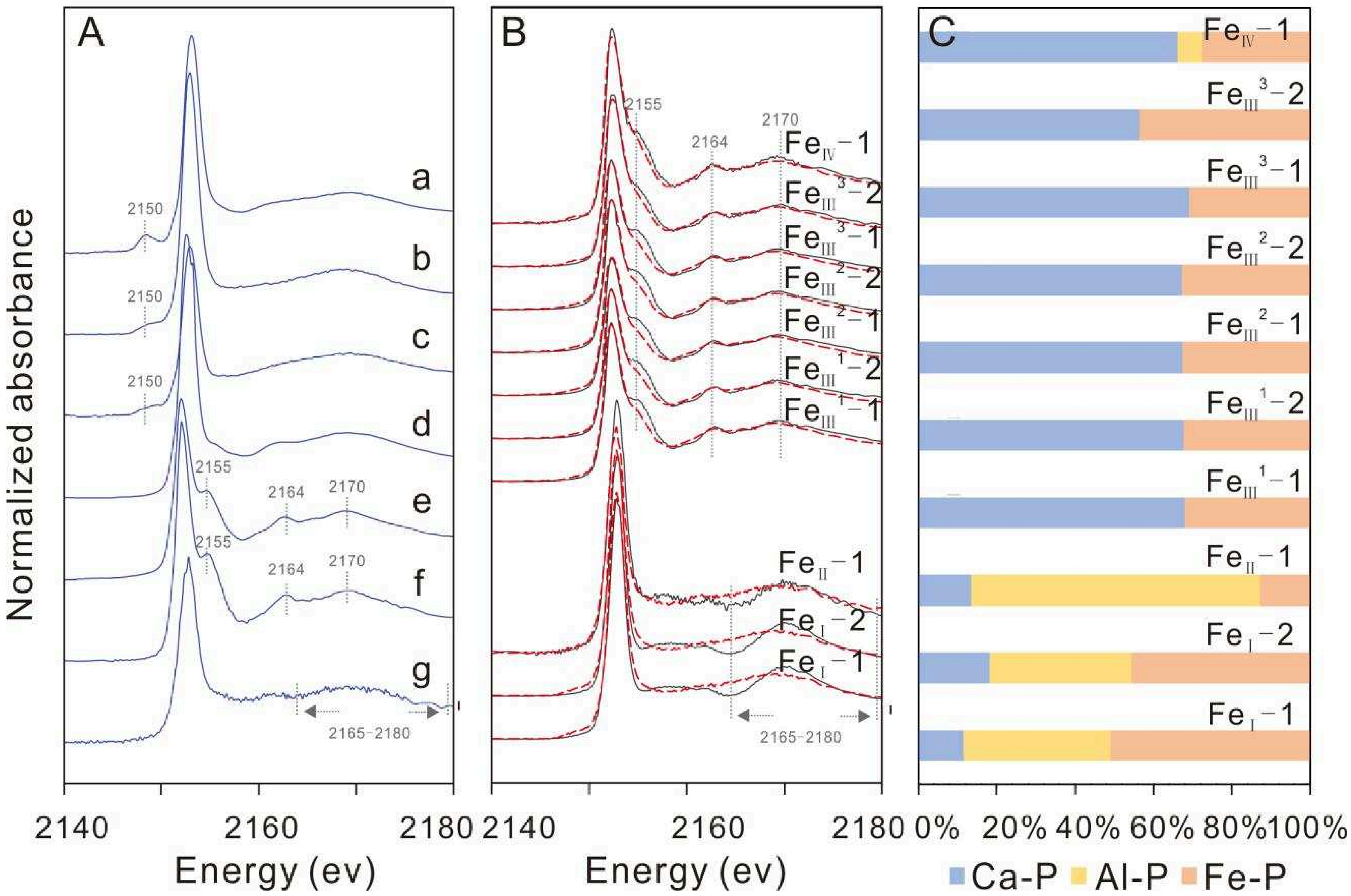

Fig. 10. Linear combination fitting results for the bulk P XANES spectra from the OIS samples. A. Several reference minerals were used for fitting: a. Amorphous $FePO_4$ (Fe-P), b. Phosphate absorbed on ferrihydrite (Fe-P), c. Strengite (Fe-P), d. Superphosphate (Ca-P), e. Octacalcium phosphate (Ca-P), f. Hydroxyapatite (Ca-P), and g. Phosphate absorbed on kaolinite (Al-P). B. Black solid lines represent the P *K-edge* X-ray absorption near edge spectra, and the red dashed lines represent the best fits obtained via linear least-squares fitting.

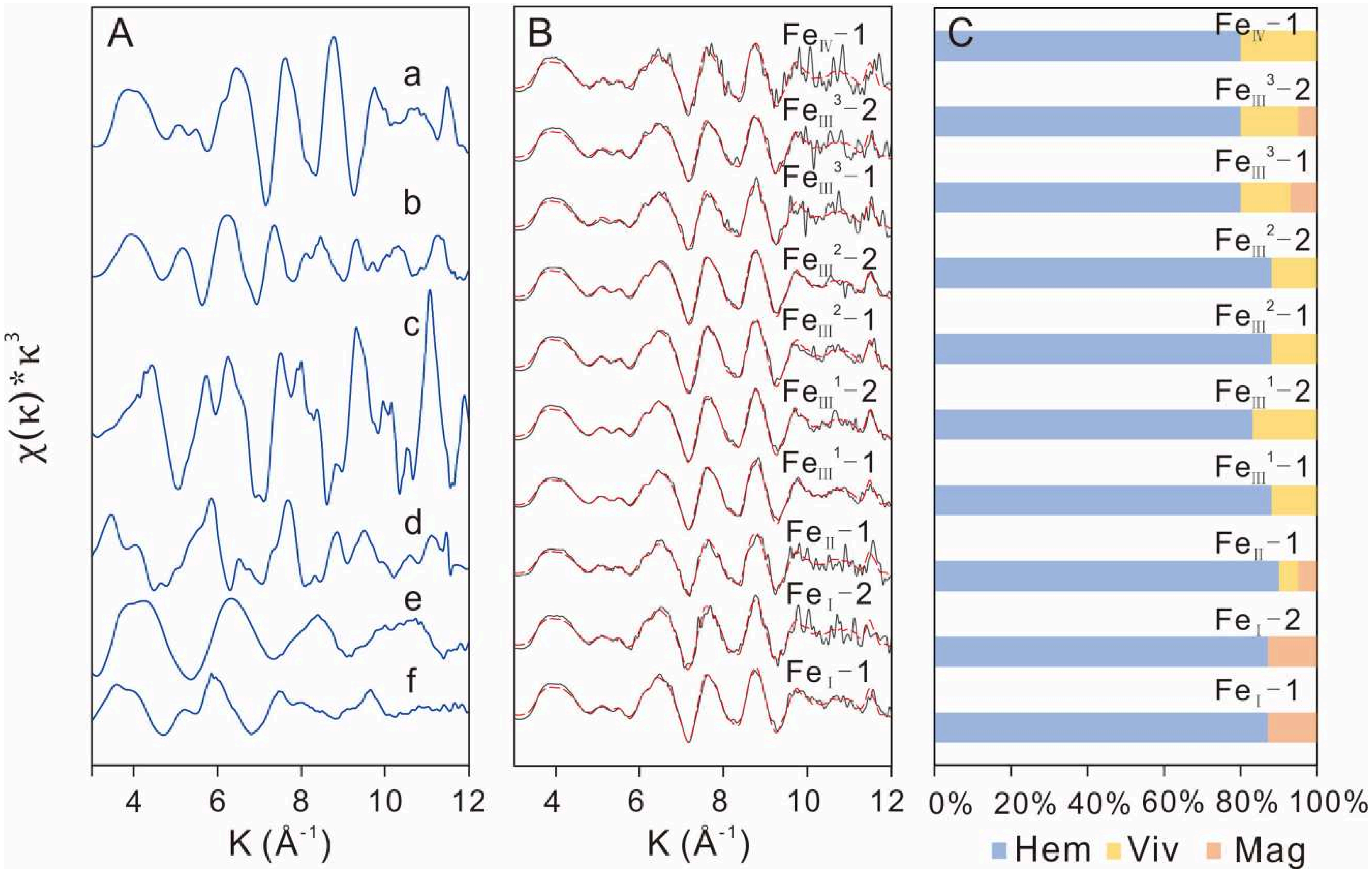

Fig. 11. Linear combination fitting results for bulk Fe *K-edge* EXAFS spectra from the OIS samples. A. k^3 weighted bulk EXAFS spectra for reference Fe compounds (a-f). a. Hematite (Fe_2O_3); b. Magnetite (Fe_3O_4); c. Pyrite (FeS); d. Siderite ($FeCO_3$); e. Strengite ($FePO_4 \cdot 2(H_2O)$); f. Vivianite ($Fe_3(PO_4)_2 \cdot 8H_2O$); B. Black solid lines represent the k^3 weighted χ-spectra, and the red dashed lines represent the best fits obtained via linear least-squares fitting; C. The percentage of Fe minerals obtained via Fe *K-edge* EXAFS.

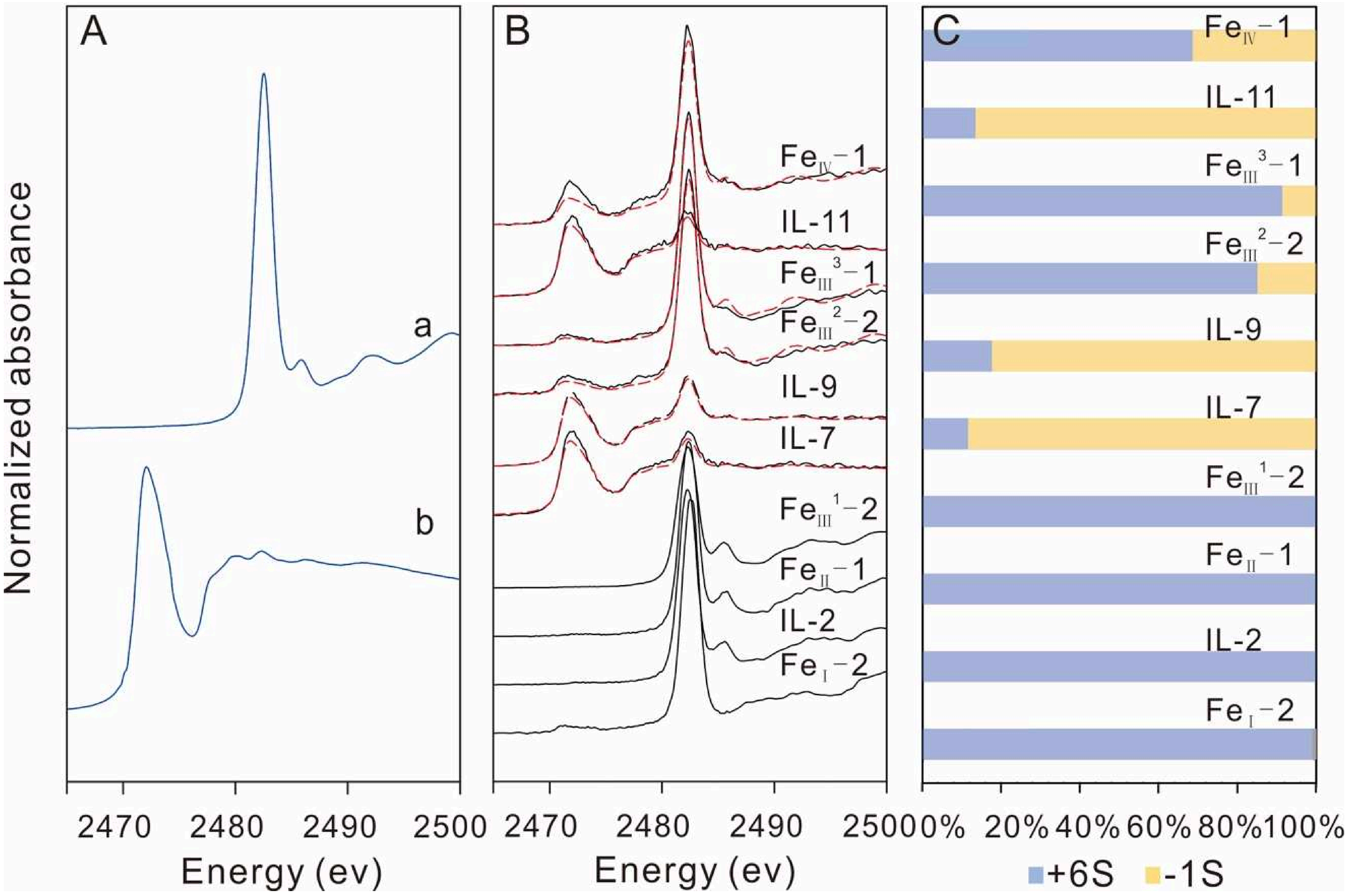

Fig. 12. Linear combination fitting results for the bulk S XANES spectra of samples from different layers. A. Gypsum (a. $CaSO_4$) and pyrite (b. FeS_2) were used for fitting; B. Black solid lines represent the S *K-edge* X-ray absorption near edge spectra, and the red dashed lines represent the best fits obtained via linear least-squares fitting. The spectra of Fe$_{I}$-2, IL-1, Fe$_{II}$-1 and Fe$_{III}^{1}$-2 were not fitted because a single gypsum peak was present in these samples. C. The percentages of gypsum and pyrite.

Table 1. Major elements and total organic carbon (TOC) contents.

Sample ID	Ca (wt%)	Al (wt%)	P_{tot} (wt%)	Fe (wt%)	TOC (wt%)
Fe_{IV}-1	26.35	1.24	0.15	14.48	0.07
IL-11	7.93	9.69	0.03	4.99	0.07
Fe_{III}^{3}-2	9.26	3.88	0.71	42.93	0.07
Fe_{III}^{3}-1	26.09	0.83	0.91	20.48	0.07
Fe_{III}^{2}-2	14.72	1.15	1.21	43.70	0.09
Fe_{III}^{2}-1	5.55	1.59	2.38	56.24	0.06
IL-10	0.87	12.11	0.67	4.65	0.20
IL-9	2.73	11.97	0.75	5.03	0.19
IL-8	0.10	9.55	0.05	2.51	0.35
IL-7	3.85	9.71	0.14	10.22	0.08
IL-6	4.12	10.79	0.14	9.84	0.08
Fe_{III}^{1}-2	9.49	1.66	1.24	39.11	0.11
Fe_{III}^{1}-1	2.79	2.29	0.92	51.24	0.09
IL-5	0.08	11.19	0.18	5.37	0.09
IL-4	0.12	8.04	0.10	1.95	0.07
IL-3	0.02	2.04	0.01	1.14	0.05
Fe_{II}-1	0.02	2.33	0.02	10.51	0.05
IL-2	0.02	1.68	0.03	8.26	0.06
IL-1	0.03	3.23	0.01	3.56	0.06
Fe_{I}-2	0.18	5.69	0.72	38.77	0.07

Table 2. P sequential extraction data for OIS and interlayer samples.

Sample ID	P_{sum} (ppm)	P_{auth} (ppm)	P_{cryst} (ppm)	P_{Ca} (ppm) [a]	P_{Fe} (ppm)	P_{org} (ppm)	Recovery (%)
$\mathrm{Fe_{IV}}$-1	1383	768	499	1267	107	8	92.37
IL-11	301	152	29	181	71	49	95.45
$\mathrm{Fe_{III}}^{3}$-2	6257	3756	2153	5909	316	32	88.55
$\mathrm{Fe_{III}}^{3}$-1	8504	6002	2223	8225	273	6	93.26
$\mathrm{Fe_{III}}^{2}$-2	10682	3734	6624	10358	311	14	88.61
$\mathrm{Fe_{III}}^{2}$-1	19575	7745	11162	18907	641	26	82.20
IL-10	6320	2947	627	3574	2598	148	94.63
IL-9	7092	3105	3654	6759	242	91	95.15
IL-8	507	138	27	165	166	177	95.30
IL-7	1245	379	704	1083	102	59	87.64
IL-6	1369	641	565	1206	100	64	94.43
$\mathrm{Fe_{III}}^{1}$-2	12109	6310	5445	11755	319	34	97.33
$\mathrm{Fe_{III}}^{1}$-1	8469	4436	3691	8127	288	53	91.67
IL-5	1607	34	26	60	1397	150	90.47
IL-4	847	49	37	86	541	220	88.06
IL-3	92	10	0	10	73	10	99.87
$\mathrm{Fe_{II}}$-1	236	85	1	86	114	36	99.52
IL-2	248	4	1	5	117	126	92.61
IL-1	124	4	0	4	72	48	99.43
$\mathrm{Fe_{I}}$-2	4940	30	28	58	911	3971	68.67

[a] P_{Ca} represents the sum of authigenic and crystalline calcium-bound phosphorus ($P_{Ca} = P_{auth} + P_{cryst}$).

Appendix

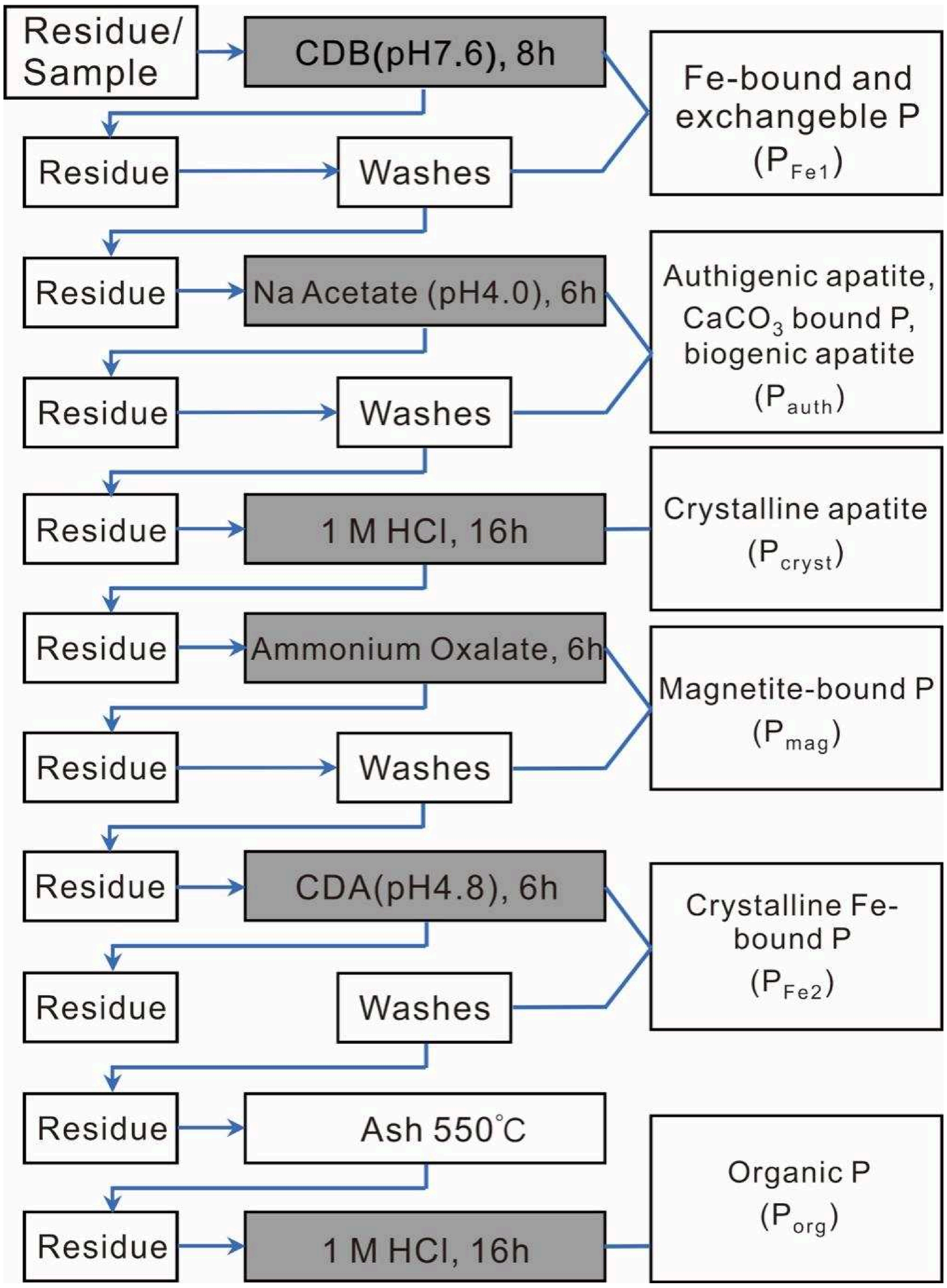

Fig. S1. Revised method for the sequential extraction of P from ancient rocks and modern iron-rich sediments (Thompson et al., 2019). P_{Fe} is the sum of P_{Fe1}, P_{mag} and P_{Fe2}. P_{cryst} includes recrystallized CFA and detrital apatite of igneous or metamorphic origin.

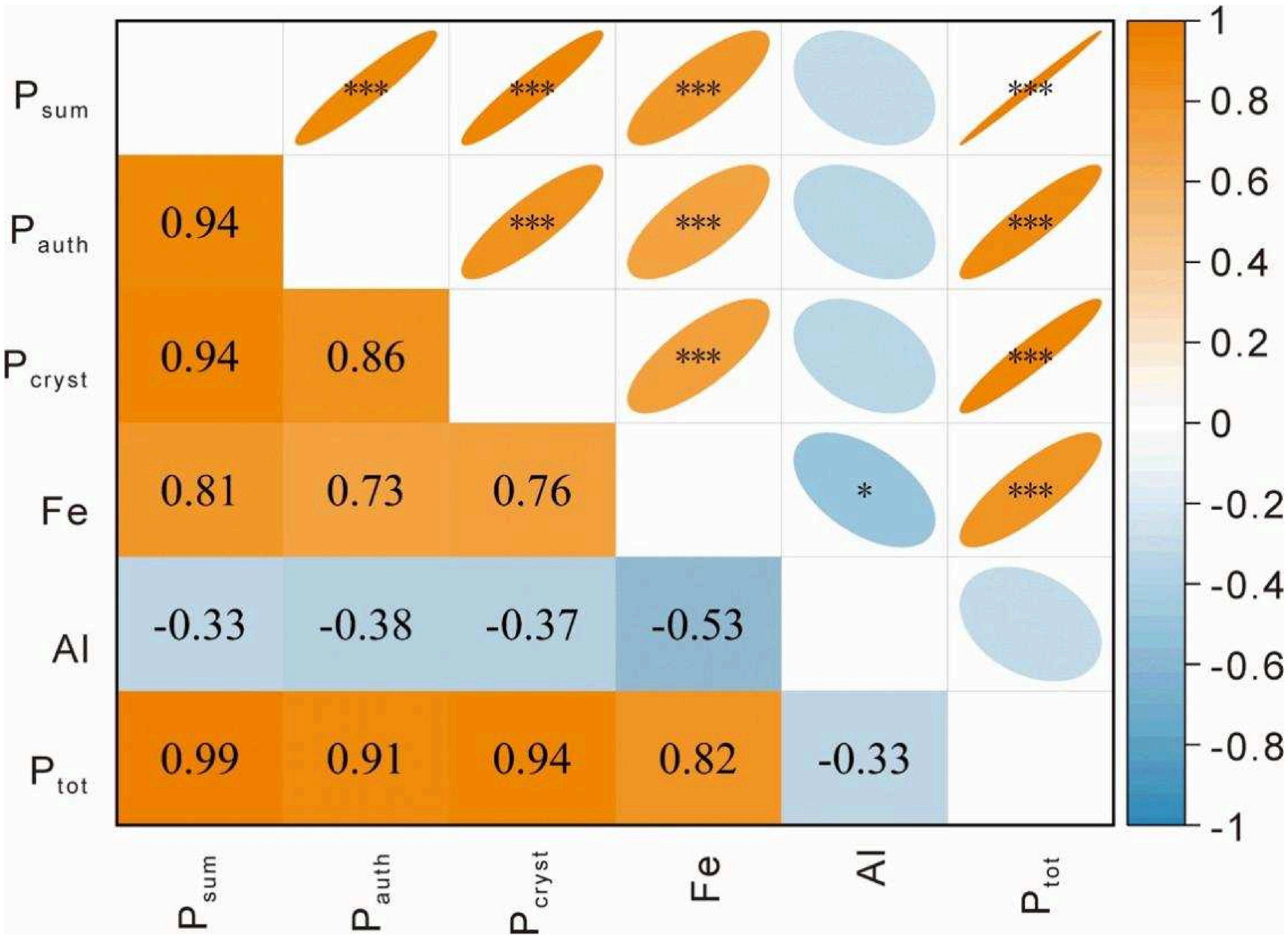

Fig. S2. Pearson correlation matrix of P phases and major element contents. P_{tot} represents total phosphorus content analysed after bulk sample digestion; P_{sum} represents the sum of phosphorus contents analysed via sequential extraction.

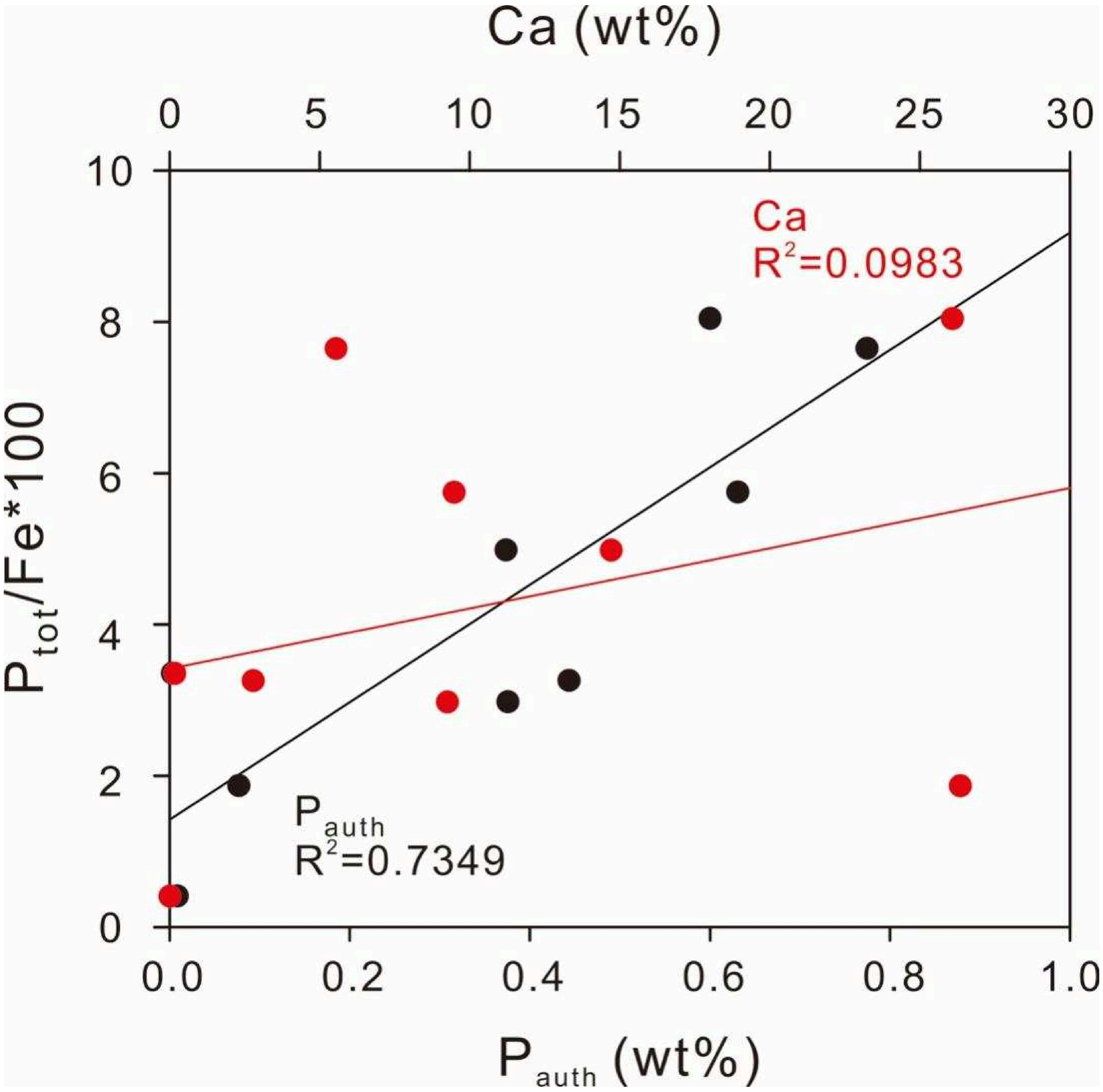

Fig. S3. Plots of bulk Ca content and authigenic calcium-bound phosphorus (P_{auth}) versus P_{tot}/Fe*100 for OIS samples, showing contrasting relationships.

Table S1. Linear combination fitting results of P *K-edge* XANES, Fe *K-edge* EXAFS, and S *K-edge* XANES spectra.

Sample ID	The percentages of Ca-P, Fe-P and Al-P via P *K-edge* XANES			The percentages of Fe minerals obtained via Fe *K-edge* EXAFS			The percentages of gypsum and pyrite via S *K-edge* XANES	
	Ca-P	Al-P	Fe-P	Hematite	Vivianite	Magnetite	Gypsum	pyrite
Fe_{IV}-1	66	6	28	80	20	0	69	31
IL-11	/	/	/	/	/	/	14	86
Fe_{III}^{3}-2	56	0	44	80	15	5	/	/
Fe_{III}^{3}-1	69	0	31	80	13	7	91	9
Fe_{III}^{2}-2	67	0	33	88	12	0	85	15
Fe_{III}^{2}-1	67	0	33	88	12	0	/	/
IL-10	/	/	/	/	/	/	/	/
IL-9	/	/	/	/	/	/	18	82
IL-8	/	/	/	/	/	/	/	/
IL-7	/	/	/	/	/	/	12	88
IL-6	/	/	/	/	/	/	/	/
Fe_{III}^{1}-2	68	0	32	83	17	0	/	/
Fe_{III}^{1}-1	68	0	32	88	12	0	100	0
IL-5	/	/	/	/	/	/	/	/
IL-4	/	/	/	/	/	/	/	/
IL-3	/	/	/	/	/	/	/	/
Fe_{II}-1	13	74	13	90	5	5	100	0
IL-2	/	/	/	/	/	/	100	0
IL-1	/	/	/	/	/	/	/	/
Fe_{I}-2	18	36	46	87	0	13	100	0
Fe_{I}-1	12	37	51	87	0	13	/	/

Table S2. Results of replicate phosphorus sequential extraction analyses for quality assessment of the SEDEX procedure.

IL-10 (ppm)	Replicate 1	Replicate 2	Replicate 3	Replicate 4	Replicate 5	Replicate 6	Average	RSD
P_{Fe1}	2518	2567	2495	2470	2542	2446	2506	1.81
P_{auth}	2966	3042	2927	2890	3005	2852	2947	2.42
P_{cryst}	630	640	624	619	635	613	627	1.61
P_{mag}	29	29	30	30	30	30	30	1.75
P_{Fe2}	64	61	62	63	63	61	62	1.94
P_{org}	156	142	145	150	153	140	148	4.30